The Pennsylvania State University

The Graduate School

DEVELOPMENT OF HIGH RELIABILITY GLASS-POLYMER LAMINATES

A Dissertation in

Materials Sciences and Engineering

by

Mengxue Yuan

Submitted in Partial Fulfillment
of the Requirements
for the Degree of

Doctor of Philosophy

May 2020

The dissertation of Mengxue Yuan was reviewed and approved by the following:

Michael T. Lanagan
Professor of Engineering Science and Mechanics
Dissertation Co-Advisor
Co-Chair of Committee

Ramakrishnan Rajagopalan
Associate Professor of Engineering
Dissertation Co-Advisor
Co-Chair of Committee

Zoubeida Ounaies
Professor of Mechanical Engineering

Qing Wang
Professor of Materials Sciences and Engineering

Susan Sinnott
Professor of Mechanical Engineering
Head of the Department of Materials Science and Engineering

ABSTRACT

Hybrid electric vehicles and plug-in hybrid vehicles require advanced technology in the areas of energy storage and power conditioning. The next-generation DC link capacitors should possess larger high field endurance and lower dielectric loss, and meanwhile be able to operate at enhanced temperatures over a prolonged service life. Recently, with the revolution in the display industry, thin films of low-alkali boroaluminosilicate glasses with excellent mechanical flexibility were produced. They can offer an outstanding level of mechanical-impact and bending strengths. Due to the lower alkali ion contents, these glasses also exhibit a large electrical breakdown strength up to 10 MV/cm, low dielectric loss, and extraordinary thermal stability (the glass transition temperature of the glasses is above 650°C). All of these attributes make low-alkali glass a promising candidate for high temperature dielectrics.

Many efforts have been devoted to exploring the breakdown mechanisms of the low-alkali boroaluminosilicate glass. It has been proposed that thermal breakdown is the main mechanism. The high field failure could also be attributed to the existence of the depletion layer. Namely, under an applied field, the sodium ions in the low-alkali boroaluminosilicate glass are driven towards the cathode side, leaving the anode region depleted of most of the ions. The substantial conductivity contrast between the depleted region and the bulk glass distorts and intensifies the local electric field in the depletion area, thus incurring the premature breakdown.

It is well known that the electrical breakdown is a stochastic process which should be best described by Weibull statistics. Beyond the characteristic breakdown strength (E_{BD}), the distribution of electrical failures — characterized by Weibull shape parameter β_w — also has important implications for the reliability and the lifetime of dielectric devices, as it is usually the low field failure that dictates the operating voltages in practical applications. Besides, the β_w shape parameter also provides and estimate of the breakdown strength of capacitor with increased size through scaling laws. The E_{BD} of

the proposed low-alkali boroaluminosiliacate glass is 10.5 MV/cm and β_w= 7. A thin layer of high glass transition temperature polymer (FPE) was coated on both sides of the glass and the polymer coating significantly increases the β_w to 49 without diluting its energy density.

Improvement of the distribution of breakdown failures necessitates the understanding of breakdown mechanisms in dielectric materials. For the low-alkali boroaluminosilicate glass system, it has been reported that the thermal breakdown is mainly responsible for the dielectric failures; other researchers have also correlated the intensified local electric fields in the ion-depleted regions with the dielectric breakdown. In this study, an alternative approach is presented to mitigate the inhomogeneous electric field distribution. Simulation result of the local electric fileld distribution supports the conclusion obtained from breakdown tests that the polymer coating reduces the enhancement of local electric field caused by local defects (sodium migration etc.) , thus eliminating the breakdown at lower electric field.

TABLE OF CONTENTS

LIST OF FIGURES

LIST OF TABLES

ACKNOWLEDGEMENTS

My deepest thanks go to my advisors Michael T. Lanagan and Ramakrishnan Rajagopalan. Not a single line in this dissertation would exist without them.

Besides my advisors, I would like to thank the rest of my dissertation committee members – Zoubeida Ounaies and Qing Wang for their great support, invaluable advice and crucial remarks that shaped my final dissertation.

I would like to thank the MRI staffs that have helped me with the experiment, especially Jeff Long, Steve Perini, and Amira Meddeb for their continuous research support. They helped me to get started in all the measurement and solved ALL the problems I encountered.

Many thanks to the individuals I have met along the way: Seth Bebano, Betul Akkopru Akgun, Eugene Furman, Mike Vecchio, Maryam Sakarat, Amir Reza, Wei Luo, Jun Gao, Zane Cohick, Hossein Hamedi, Cesar Nieves Sanabria, Wuttichai Reainthippayasakul, Roger Walker have all made my graduate school time a wonderful journey.

I am also grateful to my industrial collaborators during my internship. I spent a year at PolyK Technologies where I had the chance to collaborate with fantastic researchers. I would like to thank Shihai Zhang for providing me the great opportunity to work in his company. It was a great chance to bridge the gap between academia and industry. I also extend my gratitude to members of the team: Bo Li, Nanyan Zhang, Haijuan Zhang and Lin Nan. It was a great adventure to work with them.

Thanks are also due to the National Science Foundation (as part of the Center for Dielectrics and Piezoelectrics under grant Nos. IIP-1361571 and IIP-1361503. Partial support was also provided through the NSF PFI-AIR and INTERN programs) for their financial support that I otherwise would not have been able to develop my scientific discoveries.

Special thanks to my husband Bo Li, there is no way I could make it without his warm love, continued guidance, and endless support.

I would like to thank the two people who first showed me how to speak. Thanks mom and dad, for everything I can imagine.

Chapter 1

Introduction

1.1 Capacitors and Their Applications

Capacitors are indispensable components in many electrical and electronic applications. They can be used to store electrical charges, block DC currents while allowing AC currents to pass through (coupling), smooth output or input signals that are not at the frequency of interest (filtering) and stabilize voltage and power (decoupling).

1.2 Capacitor Candidates for Hybrid Electric Vehicles

1.2.1 Primary Capacitor Specifications

Capacitors are designed to technical specifications mainly in terms of capacitance, operating voltage, rms current, equivalent series resistance (ESR), equivalent series inductance (ESL), temperature range, and operating frequency. The primary characteristic of a capacitor is its capacitance. The capacitance of a basic parallel plate capacitor is:

$$\mathrm{C} = \epsilon_0 \epsilon_r \frac{A}{d} \qquad \textbf{1-1}$$

where C is the capacitance in Farads, ε_o is the permittivity of free space (8.85×10^{-12} F·m^{-1}), ε_r is the effective relative dielectric permittivity, A is the area and d is the dielectric thickness. Another important criterion for a capacitor is its stored energy:

$$U = \frac{1}{2} CV^2 \quad \textbf{1-2}$$

Where U is the stored energy in Joules, V is the capacitor voltage in Volts. Since the characteristic breakdown strength E_{BD} = V/d, combine **equation1-1** and **equation 1-2**, the energy stored per volume is expressed as:

$$U_{vol} = \frac{1}{2} \varepsilon_o \varepsilon_r E_{BD}^2 \quad \textbf{1-3}$$

1.1.2 Capacitor Candidates for Hybrid Electric Vehicles

1.1.2.1 Aluminum Electrolytic Capacitor

An aluminum electrolytic capacitor is a polar capacitor. The anode of the electrolytic capacitor is made of a metal material such as aluminum, tantalum, niobium, titanium, etc.; the dielectric material is a dense oxide film formed on the surface of the anode metal material; and the cathode material of the electrolytic capacitor is an electrolyte. The main feature of electrolytic capacitors is that they can get much larger capacitance than ordinary capacitors under the same volume [1-3]. Aluminum electrolytic capacitors, among other capacitors, have the highest capacitance range and outstanding volumetric efficiency [4], but the loss of liquid electrolyte over time would result in decrease in capacitance and increase in ESR [5].

1.1.2.2 Multilayer Ceramic Capacitors (MLCC)

Ceramic capacitors are ceramic-based capacitors. The structure is composed of a ceramic layer and a metal layer in which two or more layers alternately appear, and the metal layer is bonded to the electrodes of the capacitor. Usually such capacitors have excellent high frequency

characteristics and a long life. Moreover, due to the characteristics of the ceramic medium, a capacitor for manufacturing a very high voltage can be realized. However, due to the limitation of its metal layer structure, it is not suitable for long-term use under high current [6-8].

1.1.2.3 Supercapacitor

Supercapacitor is a new type of energy storage device between a conventional capacitor and a battery which has very high capacitance. Supercapacitors have a different energy storage mechanism compared to traditional capacitors [9, 10]. They store charges through a reversible redox reaction. Its performance is between that of traditional capacitors and secondary batteries, and it has higher power density than storage batteries and higher energy density than traditional electrostatic capacitors. In addition, the supercapacitor has wide operating temperature range, long service life, and introduce no pollution to the environment. It is an efficient and practical energy storage device that is convenient and environmentally friendly [11, 12]. Compared with batteries, the biggest advantage of supercapacitors is the fast charge and discharge rate. Supercapacitors can charge and discharge with a large current of several amps or even tens of amps, and can complete the charging and discharging process in tens of seconds to a few minutes; while ordinary battery charging takes several hours to complete, if charging and discharging current exceeds the limit it can also cause permanent damage to the battery [13, 14].

1.1.2.4 Polymer Film Capacitors

The film capacitor is a capacitor in which a metal foil is used as an electrode and a plastic film such as polyethylene, polypropylene, polystyrene or polycarbonate is stacked from both ends and wound into a cylindrical shape [15, 16]. The polyester material can be drawn into a film with

a thickness of a few microns, so that the insulating film of the capacitor can be obtained. In high voltage applications, polypropylene films are widely used because of their high dielectric strength and low loss factor. In order to reduce the volume of the capacitor, it is necessary to consider the thickness of the thinned electrode [15, 17, 18]. The most effective method is to use a metallized film electrode attached to the film. Since the metallization layer is extremely thin, during the electrical breakdown process, the metallization layer is vaporized during the breakdown process, so that the breakdown point electrode no longer exists, and the capacitor regains the insulation capability, it is called "self-healing" or "self-clearing" effect. When the film capacitor is operated at the rated voltage, it is necessary to ensure that any "weak point" on the insulating film is higher than the operating voltage, which means a relatively large withstand voltage margin is desired. Due to the "self-healing" capability of the metallized film, the film capacitor allows a few "weak spots" to breakdown when the voltage is applied. Thus, it is not necessary to consider an excessive withstand voltage margin in the manufacture of the film capacitor and further thins the insulating film. This not only reduces the volume of the capacitor but also reduces the cost of the capacitor [19-21]. Due to the nature of the polymer, polymer capacitor cannot be applied at high temperature, and its energy density is relatively low.

1.1.2.5 Glass Capacitor (this study)

With the revolution in the display industry, thin films of low-alkali boroaluminosilicate glasses with excellent mechanical flexibility were produced. Due to its ppm level alkali content, the majority of the high ionic conduction under electric field has been eliminated thus making it an ideal candidate for high temperature dielectric applications. Compare to MLCC capacitor, it can offer an outstanding level of mechanical-impact and bending strengths, with the ability to achieve as thin as 10 μm glass sheet commercially, bending the glass sheets into wound film capacitor is

accessible; Compare to polymer film capacitor, because of the lower alkali ion contents, these glasses also exhibit a large electrical breakdown strength up to 10 MV/cm, low dielectric loss, and extraordinary thermal stability (the glass transition temperature of the glasses is above 650 °C). As shown in **Figure 1-1**, the spider plot compares several key parameters for HEV application. All of these attributes make low-alkali glass a promising candidate for high temperature dielectrics [22-27].

In this context, we will mainly focus on the combination of the polymer film and glass sheet: polymer-glass laminate. A high energy density, high temperature endurance dielectric material with the benefit of potential enhanced mechanical property and high electrical reliability is studied for the demanding high temperature HEV capacitor applications.

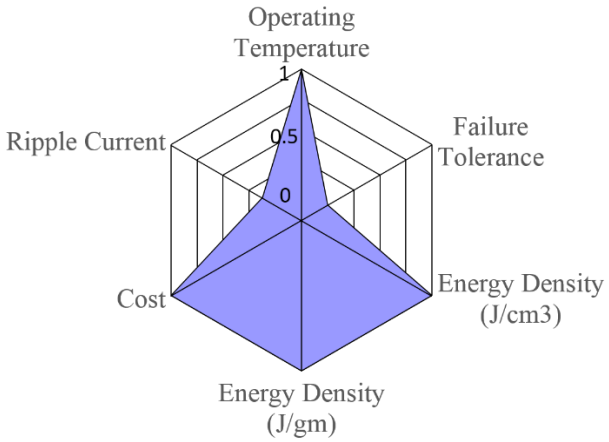

Figure 1-1: Comparison of Low-alkali Glass (OA-10G) Material Parameters

1.3 Dielectric Fundamentals

When dielectrics are subjected to an external applied electric field (E), charges can be stored on the electrode plates sandwiching the dielectrics. These charges include the contribution

from the free space (with the induced charge-density of Q) and from the dielectric materials inserted between the electrode plates (with the induced charge-density of P) (As shown in **Figure 1-2**). The ratio of the increased charges on the plates upon the inclusion of the dielectrics to the charges when the electrodes are placed in the vacuum defines the relative dielectric constant of the dielectric materials (ε) [28].

$$\varepsilon = \frac{Q+P}{Q} = \frac{\varepsilon_0 E + P}{\varepsilon_0 E} = 1 + \frac{P}{\varepsilon_0 E} = 1 + \chi \qquad \textbf{1-4}$$

Here ε_0 is the dielectric constant of the vacuum and has the value of 8.85×10^{-12} F/m^{-1}. $Q = \varepsilon_0 E$ is the stored charges when the capacitor electrodes are separated in the free space and no dielectrics are put in between; χ is the electric susceptibility of the material, indicating the degree of polarization for the dielectric material in response to an electric field. This is the fundamental dielectric equation but is only applicable for isotropic medium [28, 29].

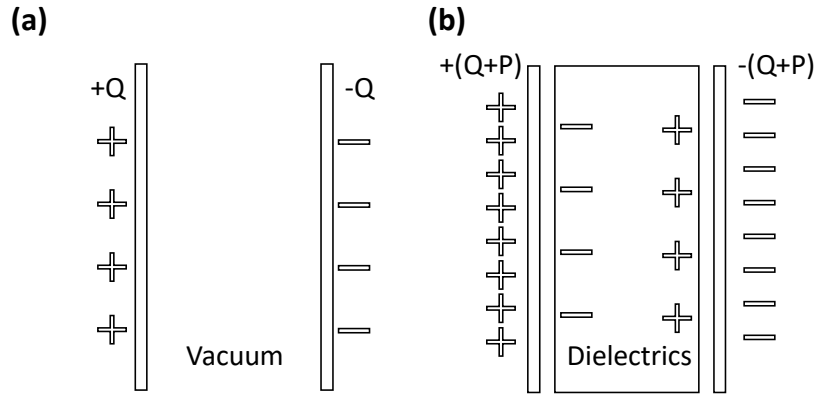

Figure 1-2: Schematic of field induced charge in dielectric material

In real dielectric materials, the internal electric field is not uniform and can exhibit strong variation especially at interfaces between the layers with different electrical properties. The polarizability of the molecules will depend on the direction of the applied field with respect to the dipole's direction of the molecules. To properly describe these anisotropic effects, the induced polarization (P) of a material should be considered on a microscopic level, which is then related to

the number density of molecules (N_0), the polarizability of the molecule (α), and the local electric field (E^L) **Error! Reference source not found.**.

$$P = N_0 \alpha E^L \quad \textbf{1-5}$$

The evaluation of the local electric field and the polarization mechanisms of a dielectric material and will be discussed in the following, respectively [30, 31].

1.3.1 Local Electric Field

As mentioned before, because of the interactions of the applied electric field with the dipoles, the internal electric field in dielectric materials will vary from point to point and be substantially different from the applied field. Generally, the local field can be calculated in a simplified model by envisaging an imaginary sphere inside the dielectric material. This sphere is small in comparison with the capacitor size, but large enough to accommodate several molecules. The local field at the point of A can be approximated by **equation 1-6**, where E^C is the electric field generated by the charges stored on the electrodes, E^P is the field from all the molecules outside the depicted sphere, and E^M is the field from the molecules inside the sphere [32].

$$E^L = E^C + E^P + E^M \quad \textbf{1-6}$$

As shown in **Figure 1-2** and **equation 1-6** , the electric field produced by the stored charges on the capacitor electrodes (E^C) can be calculated by:

$$E^C = \frac{Q+P}{\varepsilon_0} = E + \frac{P}{\varepsilon_0} \quad \textbf{1-7}$$

The electric field of E^P can be further resolved into two parts (**equation 1-8**), the contribution from the charges generated on the surface of the dielectric material ($-\frac{P}{\varepsilon_0}$) and from the surface charges of the sphere. The latter is averaged to be $\frac{P}{3\varepsilon_0}$.

$$E^P = -\frac{P}{\varepsilon_0} + \frac{P}{3\varepsilon_0} \quad \textbf{1-8}$$

The electric field of E^M is dependent on the specific molecule configuration, i.e., the alignment or arrangement of the molecular dipoles with respect to the direction of the applied field [30]. To a simplified approximation where the molecular dipoles are assumed to be randomly oriented, $E^M = 0$.

As a result, the local electric field can be obtained by **equation 1-9.**

$$E^L = E^C + E^P + E^M = E + \frac{P}{3\varepsilon_0} = \frac{\varepsilon + 2}{3}E \quad \textbf{1-9}$$

By combining **equation 1-9** with **equation 1-8** and **equation 1-7**, the famous Clausius-Mossotti equation can be derived (**equation 1-10**) [33, 34].

$$\frac{\varepsilon - 1}{\varepsilon + 2} = \frac{N_0 \alpha}{3\varepsilon_0} \quad \textbf{1-10}$$

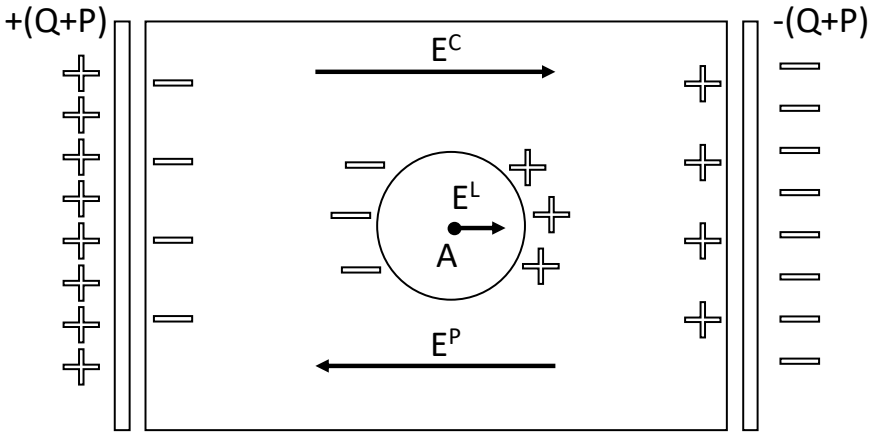

Figure 1-3: Local electric field induced from local charge movement

In the proposed polymer-glass laminate sample as introduced in Chapter 2, the polarization mechanism is composed of three parts [35]:

1) The dipole moment in polymer/glass would align with the applied electric field quickly;

2) Electrons and holes will be injected from the metal electrode (homocharges- same as the accordingly electrode) and start to accumulate around the electrode;

3) Under the applied DC electric field, the ions would move towards the electrode which has the different polarity and forms an electric double layer at the sample/metal interface. Since these ions has opposite polarity as to their compensation metal electrode, they are heterocharge.

As shown in **Figure 1-4**, the polarized dipole moment and heterocharge would generate an opposite electric field thus lowering the local electric field, which could reduce the electronic conduction in the sample; the homocharges, on the other hand, would generate an electric field that aligns with the applied electric field thus enhance the local electric field and the electronic

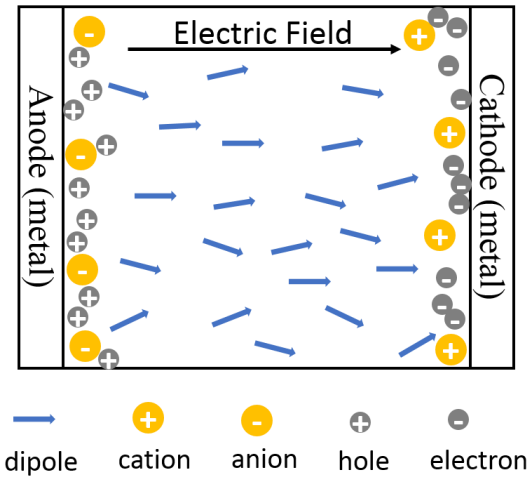

Figure 1-4: Schematic representation for polarized dipoles, injected homocharges and polarized ionic species (heterocharge) for a dielectric under a sufficiently high DC electric field.

conduction [35]. In this work, the injected electrical charge and ion conduction play important roles in the overall field distribution.

1.3.2 Polarization Mechanisms

Due to differences in composition and structure, when the external electric field is applied to the dielectric, the internal polarization mechanism can be different. Even for the same dielectric, the external electric field will induce different polarization mechanisms. From the microscopic point of view, it is generally determined by the following polarization mechanism as shown in **Figure 1-5** [29].

1.2.2.1 Electronic Polarization

At high frequency end, the electric field can displace the electrons of an atom with respect to the nucleus, causing a net dipole moment. That is to say, an induced dipole is generated due to the deviation of the center of the electron cloud from the center of the nucleus. This polarization is termed as electronic polarization, and the polarizability of a spherical atom can be approximated by $\alpha_e = 4\pi\varepsilon_0 R^3$, where R is the radius of the electron orbit. This can be intuitively expected as the bigger the size of the atom, the larger should be the electronic polarization. In general, the time required for electron polarization is about 10^{-15} s [28, 29, 31].

1.2.2.2 Ionic Polarization

With reducing frequency, the applied field can also rearrange the nuclei in a molecule. Because the heavy nuclei are slower to move around than the electrons, this polarization, also known as atomic polarization, occurs at a lower frequency region than that of the electronic polarization. Besides, the atomic polarization is usually much smaller than the electronic

polarization, with a magnitude often only one-tenth of that of the latter. In general, the time required for ionic polarization to happen is about 10^{-13} s [29, 31].

1.2.2.3 Dipolar/Orientation Polarization

The dipolar/orientation polarization is different from the first two polarization modes. In the first two polarization modes, no dipoles exist before the external electric field, and can only be induced by the external electric field. With further reducing frequency, the dielectric can demonstrate dipole polarization if there are permanent dipoles in the molecule. The dielectric itself contains the dipole, but due to the thermal energy, the dipole moment is evenly distributed in all directions, so the dipole moment vector sum of the dielectric is zero. But after the external electric field is applied, the dipole moment starts to align along the direction of the electric field and begins to appear polar. The dipolar orientational polarizability can be written by **equation 1-11**, where μ is the permanent moment of each dipole, k is the Boltzmann constant, and T the temperature.

$$\alpha_{dip} = \frac{\mu^2}{3kT} \qquad \textbf{1-11}$$

The dipole polarization is inversely proportional to the temperature, because the thermal fluctuation will disturb the dipole orientation along the electric field. It should also be noted that the dipole polarization is normally larger than the other two polarizations and can dominate and determine the polarization of polar molecules [29, 31].

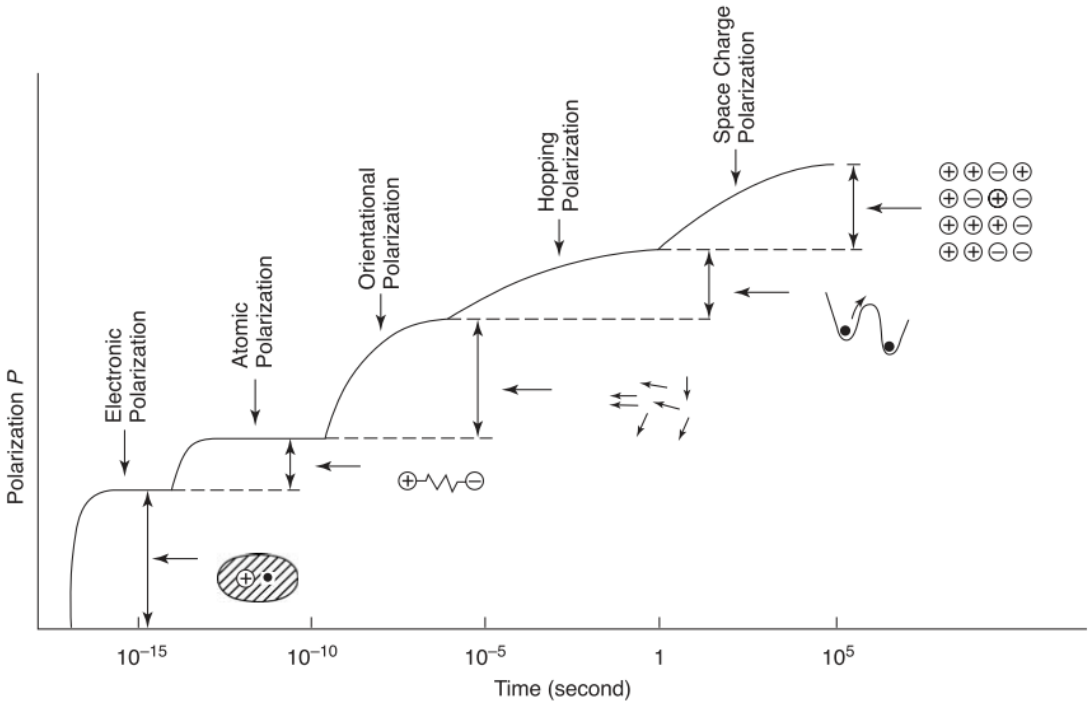

Figure 1-5: The variation of different types of polarization with time under a step-function electric field F [29].

By substituting polarizability of the Clausius-Mosotti equation (**equation 1-10**) with **equation 1-11**, the complete expression for molecular polarization can be written as:

$$\frac{\varepsilon - 1}{\varepsilon + 2} = \frac{N_0}{3\varepsilon_0}\left(\frac{\mu^2}{3kT}\right) \qquad \textbf{1-12}$$

equation 1-12 establishes the links between the microscopic molecular structures and experimentally measured macroscopic dielectric properties.

The time required for dipolar polarization is about 10^{-10}~10^{-2} s, which is greatly affected by frequency and temperature changes.

1.2.2.4 Interface Polarization

When the material is not composed of a single dielectric material, due to the difference in polarity or conductivity of different dielectric materials, the moving positive and negative ions or electrons will accumulate at the interface and cause interface polarization. The time required for interfacial polarization is longer, about 10^{-1} hours.

The dielectric relaxation mechanism of the polymer and glass in this research work will be discussed in **section 2.3.2** as well.

1.4 Problem Statement

The proposed research is to study the role of a polymer coating on the electrical field distribution and reliability of the low-alkali boroaluminosilicate glass. A series polymer- glass structure was proposed to enhance the high electric field breakdown performance thus improving the energy density of the potential high temperature dielectric for hybrid electrical vehicles. The design goal was accomplished by the following tasks:

1) Explore glass coating technologies by synthesizing a coating formula and deposition procedure to achieve the desired coating uniformity and thickness.
2) Compare the high electric field dielectric breakdown performance of a low-alkali glass with a glass-polymer laminate. Relate the improvement of electrical breakdown and Weibull modulus to the modified electric field distribution with a polymer coating.
3) Study of the role of the depletion layer underneath the coating layer and how the sodium migration and electron charge movement effects the local electric field distribution.

1.5 Original Contribution

Throughout the completion of this dissertation work, the following original contribution has been made to the field of high temperature energy storage dielectric materials:

1) *Electrical reliability improvement by polymer coating*: Some efforts have been made to study the mechanical reliability improvement of the glass material [36-38], but to the best of my knowledge, the significant Weibull modulus (β) improvement represented in **section** Error! R eference source not found. has not yet been reported. The increased β value indicates a more reliable dielectric material for potential capacitor application, since the lowest breakdown events would be significantly improved, and the laminate would have a very narrow dielectric breakdown strength range. The improved β value also has great implication on breakdown strength when scaling from lab scale to industry scale due to the scaling law.

2) *Corelate the dielectric breakdown experimental work with electric field simulation results to understand the electrical failure mode in low-alkali boroaluminosilicate glass*: The improvement of Weibull modulus after polymer coating discussed in **section** Error! Reference s ource not found. and **4.5** implied that the local electric field enhancement caused by either glass surface particle/defect or nonuniform sodium depleted region, coinciding with that obtained by simulation results in **section 5.4** and **5.5**.

1.6 References

1. Frackowiak, E. and F. Beguin, Carbon materials for the electrochemical storage of energy in capacitors. *Carbon*, 2001. **39**(6): p. 937-950.

2. Kötz, R. and M. Carlen, Principles and applications of electrochemical capacitors. *Electrochimica acta*, 2000. **45**(15-16): p. 2483-2498.

3. Gasperi, M.L. Life prediction model for aluminum electrolytic capacitors. in IAS'96. Conference Record of the 1996 IEEE Industry Applications Conference Thirty-First IAS Annual Meeting. 1996. IEEE.

4. Amaral, A.M.R. and A.M. Cardoso, A simple offline technique for evaluating the condition of aluminum–electrolytic–capacitors. *IEEE Transactions on Industrial Electronics*, 2009. **56**(8): p. 3230-3237.

5. Jeffery, J. and P. Docksey, Cost benefits of aerodynamic data generation techniques for aircraft stability and control analysis using the J2 Universal Tool-Kit. *SAE International Journal of Aerospace*, 2008. **1**(2008-01-2254): p. 636-656.

6. Kishi, H., Y. Mizuno, and H. Chazono, Base-metal electrode-multilayer ceramic capacitors: past, present and future perspectives. *Japanese Journal of Applied Physics*, 2003. **42**(1R): p. 1.

7. Pan, M.-J. and C.A. Randall, A brief introduction to ceramic capacitors. *Ieee Electrical Insulation Magazine*, 2010. **26**(3): p. 44-50.

8. Sakabe, Y., Multilayer ceramic capacitors. *Current Opinion in Solid State and Materials Science*, 1997. **2**(5): p. 584-587.

9. Conway, B.E., Transition from “supercapacitor” to “battery” behavior in electrochemical energy storage. *Journal of the Electrochemical Society*, 1991. **138**(6): p. 1539.

10. Frackowiak, E., Carbon materials for supercapacitor application. *Physical chemistry chemical physics*, 2007. **9**(15): p. 1774-1785.

11. Snook, G.A., P. Kao, and A.S. Best, Conducting-polymer-based supercapacitor devices and electrodes. *Journal of Power Sources*, 2011. **196**(1): p. 1-12.

12. Wang, G., L. Zhang, and J. Zhang, A review of electrode materials for electrochemical supercapacitors. *Chemical Society Reviews*, 2012. **41**(2): p. 797-828.

13. Zhang, L.L. and X. Zhao, Carbon-based materials as supercapacitor electrodes. *Chemical Society Reviews*, 2009. **38**(9): p. 2520-2531.

14. Zhang, L.L., R. Zhou, and X. Zhao, Graphene-based materials as supercapacitor electrodes. *Journal of Materials Chemistry*, 2010. **20**(29): p. 5983-5992.

15. Ho, J.S. and S.G. Greenbaum, Polymer capacitor dielectrics for high temperature applications. *ACS applied materials & interfaces*, 2018. **10**(35): p. 29189-29218.

16. Hudis, M. Technology evolution in metallized polymeric film capacitors over the past 10 years. in CARTS-CONFERENCE-. 1996. COMPONENTS TECHNOLOGY INSTITUTE INC.

17. Ho, J.N. and T.R. Jow, High Field Conduction in Biaxially Oriented Polypropylene at Elevated Temperature. *IEEE Transactions on Dielectrics and Electrical Insulation*, 2012. **19**(3): p. 990-995.

18. Liu, Y., T. Cui, and K. Varahramyan, All-polymer capacitor fabricated with inkjet printing technique. *Solid-State Electronics*, 2003. **47**(9): p. 1543-1548.

19. Manoharan, M., et al. High temperature-High energy density polymer-coated glass capacitors. in Transportation Electrification Conference and Expo (ITEC), 2013 IEEE. 2013. IEEE.

20. Tan, D., et al., High-Temperature Capacitor Polymer Films. *Journal of Electronic Materials*, 2014. **43**(12): p. 4569-4575.

21. Wang, Y., et al., Recent development of high energy density polymers for dielectric capacitors. *IEEE Transactions on Dielectrics and Electrical Insulation*, 2010. **17**(4): p. 1036-1042.

22. Patey, T.J., C. Schlegel, and E. Logakis, Glass as dielectric for high temperature power capacitors. *MRS Proceedings*, 2014. **1679**.

23. Smith, N.J., et al., Alkali-free glass as a high energy density dielectric material. *Materials Letters*, 2009. **63**(15): p. 1245-1248.

24. Manoharan, M.P., et al., Flexible Glass for High Temperature Energy Storage Capacitors. *Energy Technology*, 2013. **1**(5‐6): p. 313-318.

25. Lee, H., et al., Dielectric breakdown of thinned BaO–Al2O3–B2O3–SiO2 glass. *Journal of the American Ceramic Society*, 2010. **93**(8): p. 2346-2351.

26. Lee, H. and M.T. Lanagan, Dielectric-breakdown and conduction-mechanism in a thinned alkali-free glass. *Journal of the Korean Physical Society*, 2014. **65**(7): p. 955-959.

27. Smith, N.J., M.T. Lanagan, and C.G. Pantano, Thermal poling of alkaline earth boroaluminosilicate glasses with intrinsically high dielectric breakdown strength. *Journal of Applied Physics*, 2012. **111**(8): p. 083519.

28. Kasap, S.O., Principles of electronic materials and devices. Vol. 81. 2006: McGraw-Hill New York, NY.

29. Kao, K.C., Dielectric phenomena in solids. 2004.

30. Seanor, D.A., Electrical properties of polymers. 2013: Elsevier.

31. Jonscher, A.K., Dielectric Relaxation in Solids. 1983: Chelsea Dielectrics Press.

32. Yang, L., et al., Perovskite lead-free dielectrics for energy storage applications. *Progress in Materials Science*, 2018.

33. Jonscher, A.K., Electronic properties of amorphous dielectric films. *Thin Solid Films*, 1967. **1**(3): p. 213-234.

34. Callister, W.D. and D.G. Rethwisch, Materials science and engineering: an introduction. Vol. 7. 2007: Wiley New York.

35. Yang, L., et al., Semicrystalline structure–dielectric property relationship and electrical conduction in a biaxially oriented poly (vinylidene fluoride) film under high electric fields and high temperatures. *ACS applied materials & interfaces*, 2015. **7**(36): p. 19894-19905.

36. Kendall, K., et al., Influence of toughness on Weibull modulus of ceramic bending strength. *Journal of Materials Research*, 1986. **1**(1): p. 120-123.

37. Roy, A., et al., Improvement in mechanical properties of jute fibres through mild alkali treatment as demonstrated by utilisation of the Weibull distribution model. *Bioresource technology*, 2012. **107**: p. 222-228.

38. Sarkarat, M., et al., Enhanced mechanical stability of high temperature ultra-thin glass/polymer composite dielectrics. *Materials Letters*, 2017. **208**: p. 10-13.

Chapter 2

Sample Fabrication and Experimental Procedure

2.1 Introduction

The content of this chapter is composed of two sections. **Section 2.2** describes the procedure followed to fabricate the proposed polymer-glass laminate. In this section, the reason of choosing this polymer and its thermal and dielectric properties has been explained. The coating procedure and how to achieve a uniform coating film on top of glass has also been discussed here, including the failed solutions. The morphology characterization of the polymer coating showing its thickness, uniformity and content are introduced in **section 2.3.1**, both Scanning Electron Microscope (SEM) and Fourier-transform Infrared Spectroscopy (FTIR) has been utilized to characterize the laminate. Then in the remaining content of the **section 2.3** the fundamentals of several dielectric characterization analysis method - dielectric relaxation spectroscopy (DRS), impedance spectroscopy(IS), thermally stimulated depolarization current (TSDC) and dielectric breakdown – are briefly introduced , together with how these analysis method would be used in this study. It is not necessary for informed readers to go through this section to understand the following chapters.

2.2 Sample Fabrication

Fluorene polyester (FPE, 9,9-bis[(4-hydroxyphenyl)fluorene],1,4-benzenedicarbonyl dichloride 1,3-benzenedicarbonyl dichloride copolymer, CAS No: 28906-27-6, Ferrania Technologies, the chemical structure is shown in **Figure 2-1**) was chosen as the coated polymer

due to its high glass transition temperature and low dissipation factor. The Differential Scanning Calorimetry (DSC) result (Error! Reference source not found.**a**) shows that the glass transition t emperature (T_g) of the polymer is 326 ^oC. Thermogravimetric analysis (TGA) result shown in **Error! Reference source not found.b** shows the thermal stability of the FPE polymer resin in air (heating rate 5^oC/min), the FPE starts to oxidize at 419 ^oC. The FTIR spectrum shown in Error! Reference source not found.**c** indicates the existence of the carbonyl (C=O) absorption between 1690- 1760 cm^{-1} and C-O absorption between 1080 and 1300 cm^{-1} after 5 min high temperature treatment up to 500^oC in air of ~5 μm FPE film.

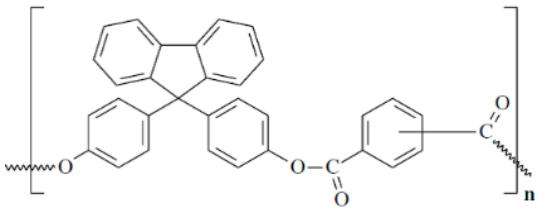

Figure 2-1: Chemical structure of fluorene polyester

The fundamental factors that led to a good coating were adhesion, wetting and surface preparation. For our particular glass (OA-10G, NEG®) and FPE polymer, the polar bonding (hydrogen bonding and Van der Waals force) was the most possible adhesion mechanism, instead of the primary bonding (which requires the bonding, ionic or covalent, that holds molecules between glass and polymer) or mechanical forces (for rough surfaces). Regardless of what type of bonding exist in the interface, the ability of the coating to create an intimate physical $\cos\theta = \Upsilon_{sl} - \Upsilon_{sv}$, if the surface tension of the coating (Υ_{sl}) was much less than the critical surface tension of the substrate (Υ_{sv}), then the polymer/solvent liquid could wet the substrate completely (contact angle θ equals 0) as shown in **Figure 2-3**. **Table 2-1** lists the surface tension of three major solvents that can dissolve the FPE [1]. Besides these two factors, the cleanness of the substrate surface also affects the coating performance. For instance, the oil or grease may lower the surface tension of the substrate thus inhibiting the wetting to occur [2].

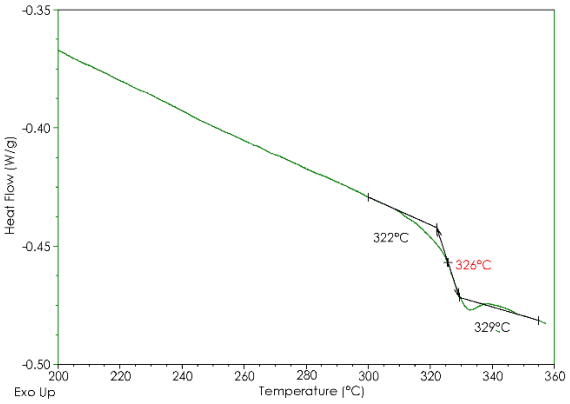

(a)

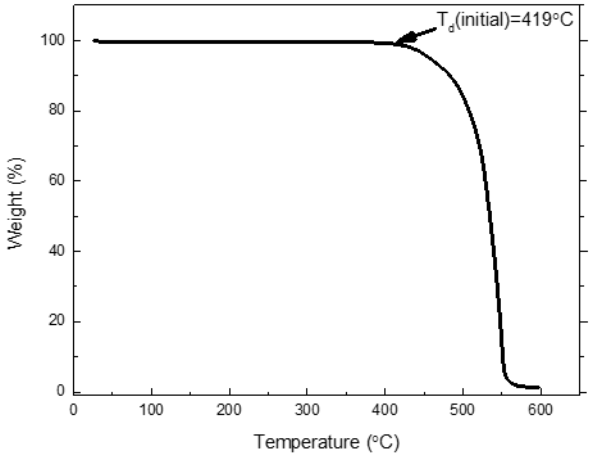

(b)

Figure 2-2: (a) Differential Scanning Calorimetry (DSC) result of FPE polymer (b) Thermogravimetric analysis (TGA) of the FPE polymer.

Dip coating was chosen due to its low cost, suitability for handling fragile glass and ability to produce coatings in the desired thickness range (~1 μm). In this process, the substrate was successively dipped into the solution and withdrawn at a constant speed (**Figure 2-4a**) [3]. The

thickness of the coating was a function of the withdraw speed, the evaporation speed of the solvent, and the viscous drag (balanced at stagnation point as shown in **Figure 2-4b**) [3-7].

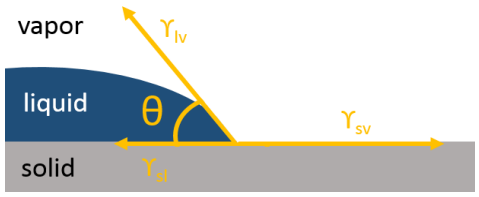

Figure 2-3: Contact angle measurement

Table 2-1. Solvent surface tension

Solvent	Surface Tension (dyne/cm) @20°C
Tetrahydrofuran (THF)	28
Dimethylformamide (DMF)	35
N-Methyl-2-pyrrolidone (NMP)	40.7

Every coating was an optimization of several parameters,

Figure 2-4: (a)Dip Coating Process and (b) the balance of the driving forces

Table 2-2 lists the coating parameters that resulted in an uniform coating. The mixed solvent is chosen due to a combination of solubility, surface tension, viscosity and evaporation rate. Single solvent had been tested but resulted in crawling (solution retracts from the glass substrate [8]). 1wt.%, 2wt.%, 3wt.% and 5wt.% concentration had been tested and the 3wt% concentration generated the most uniform film, the resin concentration could affect the solution viscosity and surface tension. The dragging speed of 10, 15 and 20 cm/s had been tested, it mostly affects the

desired thickness and coating uniformity, faster speed tends to generate a thinner coating [9] but may leave a drop of solution on the bottom of the dipped sample due to gravity. The dip coated sample was left to dry at an elevated temperature in order to avoid moisture penetration into the freshly coated layer, resulting in a cloudy film (FPE polymer cannot dissolve in water thus precipitated out) [10].

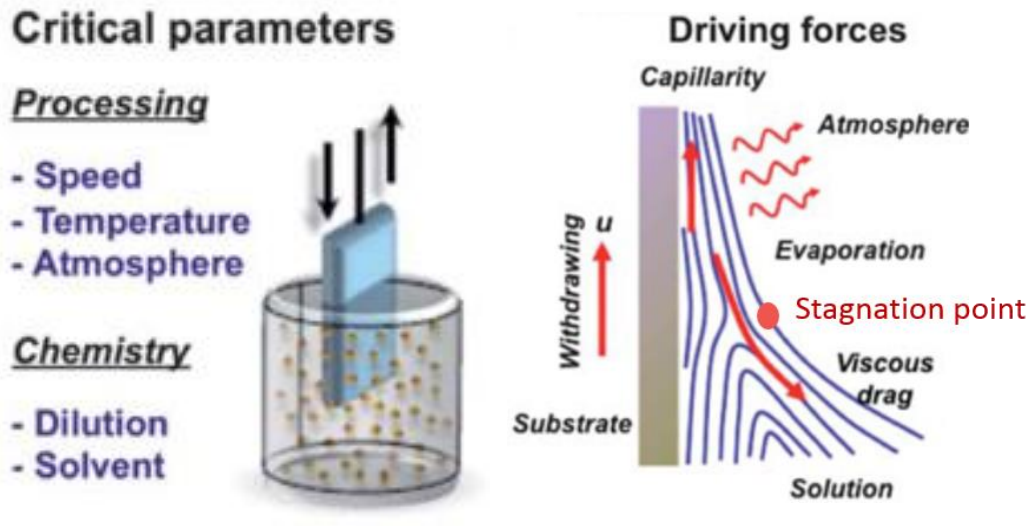

(a) (b)

Figure 2-4: (a)Dip Coating Process and (b) the balance of the driving forces

Table 2-2: Coating Parameters

Conditions	Parameters
Solvent	THF/NMP = 1:9
Concentration	3 wt.%
Viscosity	10.9 CPS
Estimated Speed	15cm/s
Drying Temperature	130^{o}C

The ultimate coating procedure starts with dissolving a 3wt.% of FPE resin in a solvent mixture of 90vol% *N*-Methylpyrrolidine (NMP, 97% purity, SIGMA-ALDRICH®) and 10wt.% tetrahydrofuran (THF 99.9% purity, SIGMA-ALDRICH®). The solution was then stirred by a magnetic stirrer for 4hrs to completely dissolve the FPE resin. After clean the glass with air gun to blow away surface particles (to avoid cratering - a hydrophobic contaminant induces flow of solution during film formation), the trimmed glass was then coated with FPE by dipping the glass into the solution and dragged out at a constant speed; finally, the laminate was hung in a gravity oven for drying at 130 ^{o}C for 18 hrs.

2.3 Experimental Procedure

2.3.1 Sample Structure Characterization

The laminate structure of the polymer-coated glass is investigated by the cross-section SEM images as shown in **Figure 2-5a**, where a uniform polymer layer with a thickness of ~400 nm can be identified on top of the glass substrate, with a 10% error (compared to the result of a TMG universal benchtop material thickness gauge 0.0002 mm resolution). It is consistent with FTIR comparison between the pristine and the polymer-coated glasses (**Figure 2-5b**). The characteristic bands of the polymer, i.e., aromatic C-H stretching (3000-3100 cm^{-1}) and ester aliphatic C=O stretching (1735-1750 cm^{-1}), appear on the laminate, but are absent from the uncoated glass.

2.3.2 Dielectric Relaxation and Spectroscopy

In **Polarization** Mechanisms, the four common polarization mechanisms had been discussed in Chapter 1. Here specific polarization mechanisms are outlined for glass and polymer, For glass material, the glass network former (SiO_2, B_2O_3, GeO_2, etc.) contributes to the dipolar polarization and the glass modifier oxide such as Na_2O, Li_2O, BaO, CaO etc. that modifies the most of the physical, chemical, thermal and electrical of the glass is ionic polarization. The dielectric constant of the proposed OA-10G glass in this study is 5.3 (25 ^oC, 1 MHz), though it's low-alkali glass, but the trace amount of Na^+ (100 ppm) still contribute to its permittivity, especially at low frequency and high temperature.

For polymer material, dipolar polarization contributes the most to the total polarization. Depending on the effective dipole moment of the various groups in the polymer, the polymers can be classified by polarity- from non-polar (polyethylene, polypropylene, etc.) to polar (polyethylene terephthalate, polyvinyl alcohol, etc.). The FPE polymer in this study is a polar molecule as shown in **Figure 2-1**, and its dielectric constant is 3.2 (25 ^oC, 1 MHz). In **section 3.2**, the dielectric relaxation spectroscopy will be utilized to study the dielectric constant/permittivity and loss/dissipation factor of the glass and polymer-glass laminate.

2.3.3 AC Impedance Spectroscopy

Impedance spectroscopy (IS) has firmly established itself as one of the most informative and irreplaceable investigation methods in the fields of physical chemistry, electrochemistry or physics. It is the method of choice for characterizing the electrical behavior of interfaces though various conductivity contribution [11]. In IS study, the test material is regarded as an equivalent circuit composed of basic components such as resistor, capacitor, and inductor in series or in

parallel, and can be combined by IS. The composition of the equivalent circuit and the size of each element were measured, and the physical meaning of these elements was used to analyze the structure of the material.

In AC circuit, the complex impedance can be written as:

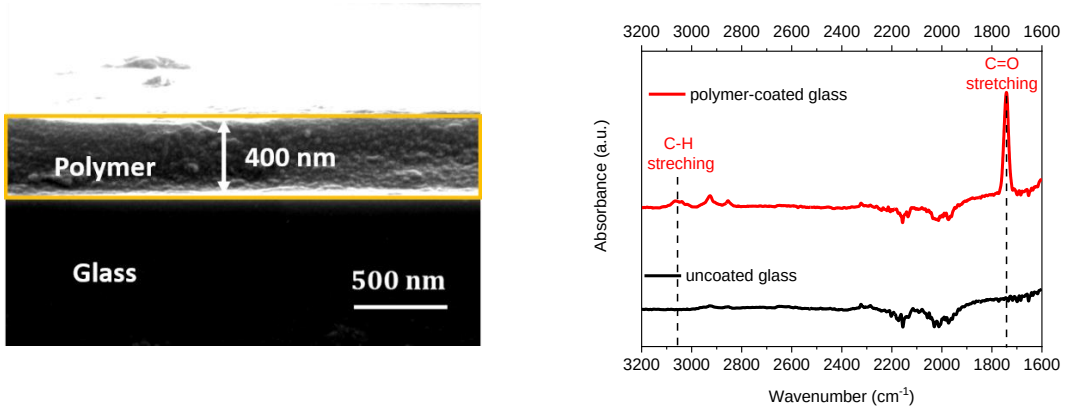

(a) (b)

Figure 2-5: (a) SEM of the dip coated laminate (cross section); (b) FTIR of the uncoated glass and polymer-coated glass.

$$Z(\omega) = Z' - jZ'' \quad \textbf{2-1}$$

In which ω is the angular frequency, Z' and Z'' are the real part and imaginary part of the complex impedance respectively, and j is the imaginary number. The vector quantity is plotted in the plane as in **Figure 2-6** [11]. When a vector is represented on the coordinate system, the real part is usually the horizontal axis and the virtual part is the vertical axis. The vector length from the origin to a certain point (Z', Z") is the modulus of the impedance Z, and the angle θ is the phase angle of the impedance. The modulus of the impedance is:

$$|Z| = \sqrt{Z'^2 + Z''^2} \quad \textbf{2-2}$$

and the phase angle is:

$$\theta = tan^{-1}(Z''/Z') \quad \textbf{2-3}$$

Thus Z' and Z'' can be represented as:

$$Z' = |Z|cos(\theta) \quad and \quad Z'' = |Z|sin(\theta) \qquad \textbf{2-4}$$

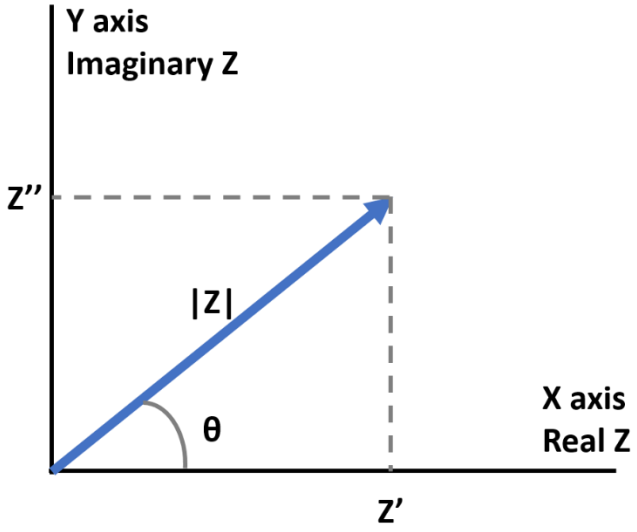

Figure 2-6: The complex impedance Z plotted as a planar vector using rectangular and polar coordinates.

The design of AC Impedance Spectroscopy is to generate a small AC signal (excluding any electronic contribution to conduction, only linear behavior is implied) and measure the response of the current and its phase angle changing with input frequency. Thus, the Z', Z" and its modulus and phase angle can be achieved and plotted in Nyquist plot/Cole-Cole plot (Z' and Z'' are the x axis and y axis respectively, as shown in **Figure 2-7** form to be analyzed [12].

(a) Resistor (R)

For an ideal resistor with a resistance of R, Z' = R, Z"= 0 (no imaginary part). It can be represented by a single dot on the x axis as in **Figure 2-7a**.

(b) Capacitor (C)

For an ideal capacitor with a capacitance of C, Z' = 0 (no real part), Z"= 1/iωC. It can be represented by a vertical line on the y axis as in Figure 2-7b.

(c) RC in parallel

$$\frac{1}{Z(\omega)} = \frac{1}{Z(\omega)_R} + \frac{1}{Z(\omega)_C} = \frac{1}{R} + j\omega C = \frac{R}{1+(\omega RC)^2} - j\frac{\omega R^2 C}{1+(\omega RC)^2} \quad \textbf{2-5}$$

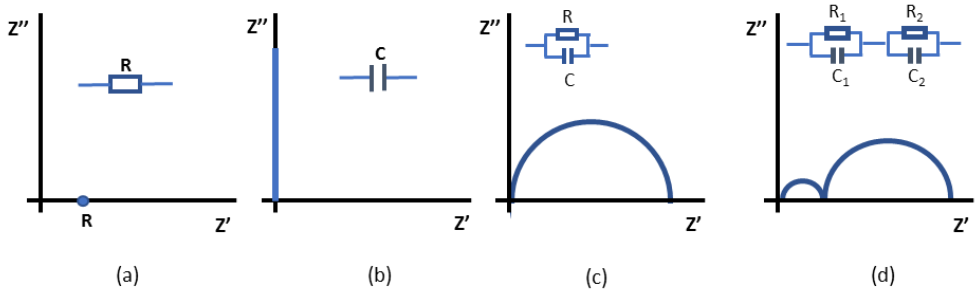

Figure 2-7: Schematic of ideal typical Nyquist plot of equivalent circuit. (a) resistor; (b)capacitor; (c) resistor and capacitor in parallel; (d)double resistor and capacitor in parallel.

$$Z' = \frac{R}{1+(\omega RC)^2} \quad \textbf{2-6}$$

$$Z'' = \frac{\omega R^2 C}{1+(\omega RC)^2} \quad \textbf{2-7}$$

Combine **equation 2-6** and **equation 2-7**Error! Reference source not found.:

$$(Z' - \frac{R}{2})^2 + Z''^2 = (\frac{R}{2})^2 \quad \textbf{2-8}$$

It can be represented by a semicircle with its center on (R/2, 0) and a radius of R/2 as shown in **Figure 2-7c**. The measured curve usually deviates from the semicircular trajectory and appears to be a circular arc. It reflects the nature of the material deviating from the ideal capacitator. That is to say, it is not accurate enough to simply substitute the material as a physical pure capacitance type, and it is widely represented by a constant phase element (CPE) element in the equivalent circuit model.

(d) Double parallel RC in series ($R_1<R_2$, $C_1<C_2$)

The complex impedance for this double parallel RC in series circuit is written as:

$$Z(\omega) = (\frac{1}{R_1} + j\omega C_1)^{-1} + (\frac{1}{R_2} + j\omega C_2)^{-1} = Z' - jZ'' \quad \textbf{2-9}$$

where

$$Z' = \frac{R_1}{1+(\omega R_1 C)^2} + \frac{R_2}{1+(\omega R_2 C)^2} \quad \textbf{2-10}$$

and

$$Z'' = R_1\left(\frac{\omega {R_1}^2 C}{1+(\omega R_1 C)^2}\right) + R_2\left(\frac{\omega {R_2}^2 C}{1+(\omega R_2 C)^2}\right) \quad \textbf{2-11}$$

It can be represented by a double semicircle with the first center on (R_1/2, 0) and a radius of R_1/2, and the second center on (R_1+ R_1/2) and a radius of R_2/2 as shown in **Figure 2-7d**.

In **section 3.3**, the impedance spectroscopy will be utilized to differentiate the bulk of the glass and the sodium depleted region and calculate their thickness.

2.3.4 Thermally Stimulated Depolarization Current (TSDC) Measurements

The thermal stimulation method is different from the previous material parameters measurement. In the past, mostly the material parameters are measured when the temperature is kept constant, i.e., isothermal measurement, and thermal stimulation is a measurement of the material during the temperature rise, i.e., non-isothermal measurement. Since the microscopic parameters (such as activation energy H, relaxation time τ, etc.) of the charged particles in the material (such as dielectric material) are different, thermal stimulation is a convenient tool to separate the charged particles with different H or τ in the material to find the respective parameters. Since the thermal stimulation current is closely related to these parameters of the material, it is an effective way for studying dielectric materials, insulating materials, semiconductor materials, and so on [13-19].

TSDC measurement method: Firstly, the dielectric sample is applied with a strong static electric field E at an elevated polarization temperature T for polarization, and after a certain polarization time, the sample is rapidly quenched under the condition that the electric field strength is constant. At low temperature, the electric field is removed, thus an electret is formed, and then

the sample is heated at a constant ramping rate. A pA meter is directly connected to both ends of the sample to measure the released current, and the electret is heated at the linear temperature ramping hate to a temperature below its melting point. The TSDC spectrum collected by the computer is the temperature-dependent release current spectrum of the sample formed in the external circuit. **Figure 2-8a** is a schematic diagram of thermal stimulated polarization current measurement [18, 19].

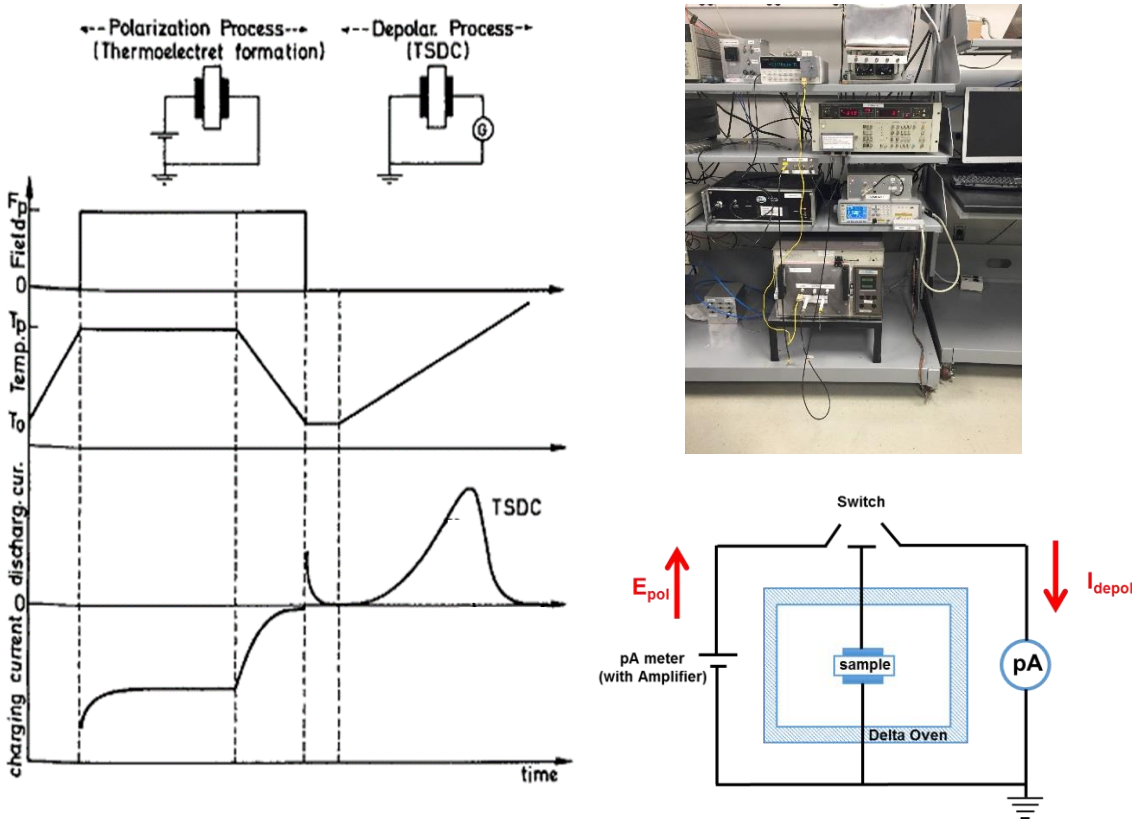

(a) (b)

Figure 2-8: (a) Schematic of Polarization and Depolarization of the TSDC Process [13] and (b)TSDC instrument and a schematic figure.

The Bucci-Fieschi theory is used to describe the dipole relaxation process [13, 17]. Assuming that a thermal electret is prepared under polarization states of T_p, E_p, and t_p, the polarization intensity changes with time:

$$\frac{dP(t,T)}{dt} = -P(t,T)/\tau(T) \quad \textbf{2-12}$$

where t is the relaxation time, and the relationship between polarization and temperature can be expressed by the Arrhenius equation:

$$\tau(T) = \tau_0 exp(E_a/kT) \quad \textbf{2-13}$$

where τ_0 is the relaxation time, E is the activation energy, and k is the Boltzmann coefficient.

equation 2-13 is changed to:

$$P(t,T) = P_0 exp(-\int \frac{dt}{\tau(t,T)}) \quad \textbf{2-14}$$

In which the initial polarization in the equation is:

$$P_0 = N\mu^2 E_p \alpha/kT_p \quad \textbf{2-15}$$

where N is the dipole concentration, μ is the dipole moment, and a is the shape parameter. During thermal relaxation, the current is:

$$I(t,T) = -\frac{dP(t,T)}{dt} = \frac{P_0}{\tau} exp(-\int \frac{dt}{\tau(t,T)}) \quad \textbf{2-16}$$

When the temperature ramping rate of the test increases linearly:

$$T = T_0 + \beta t \quad \textbf{2-17}$$

Where T_0 is the initial temperature. Then general equation for the dipole thermal relaxation process is:

$$I(T) = \frac{P_0}{\tau} exp[-\frac{E_a}{kT} - \frac{1}{\beta\tau_0}\int_{T_0}^{T} exp(-\frac{E_a}{kT})dT] \quad \textbf{2-18}$$

The measured depolarization current is a net charge often consists of two opposite charges depending on their polarity in regard of the adjacent forming electrode. Homo-charge arise from the same polarity (positive charge adjacent from the anode or negative charge adjacent from the

cathode), and hetero-charge the opposite polarity. In this study, the depolarization current (I_{depo} as shown in **Figure 2-8b**) with the same polarity as to the polarization current is characterized as hetero-charge. In a previous study of our group [20], the TSDC method has been utilized to study the high electric field conduction mechanism of the glass. In this study the TSDC hetero-charge will be discussed in **Chapter 4**, it was used to confirm the Poole-Frenkel conduction mechanism in sodium depleted region and illustrate the electric field reinforcement in this region.

2.3.5 Dielectric Breakdown

The dielectric material can maintain its insulation and store charge only within a certain electric field. When the applied electric field strength exceeds a certain critical value, the dielectric changes from a dielectric state to a conductive state. This failure is the breakdown of the medium. At the time of breakdown, the applied voltage is called the breakdown voltage, and the corresponding electric field strength is called the breakdown field strength or dielectric strength. For solid dielectrics, localized high temperatures are generated due to the sharp increase in current through the material during breakdown, resulting in through-holes, cracks, and even bursts at the point of breakdown, resulting in irreversible permanent damage to the material itself. Therefore, in many cases, the breakdown field strength becomes one of the thresholds determining the life of the electronic equipment. The breakdown of solid dielectrics is mainly divided into electrical breakdown, thermal breakdown, electromechanical breakdown and partial discharge breakdown [21, 22]. **Figure 2-9** shows the times and electric field at which various electrical breakdown mechanisms are operative [23].

Some initial electrons in the dielectric transfer the electric field energy to the crystal lattice by the action of the external electric field. When the electric field strength exceeds a certain value, the collision initiation ionization begins in the dielectric, and the carrier concentration increases

rapidly until it is sufficient to destroy the medium, causing loss of its insulating properties and breakdown. A schematic process of electrical breakdown in shown in **Figure 2-10a** [24].

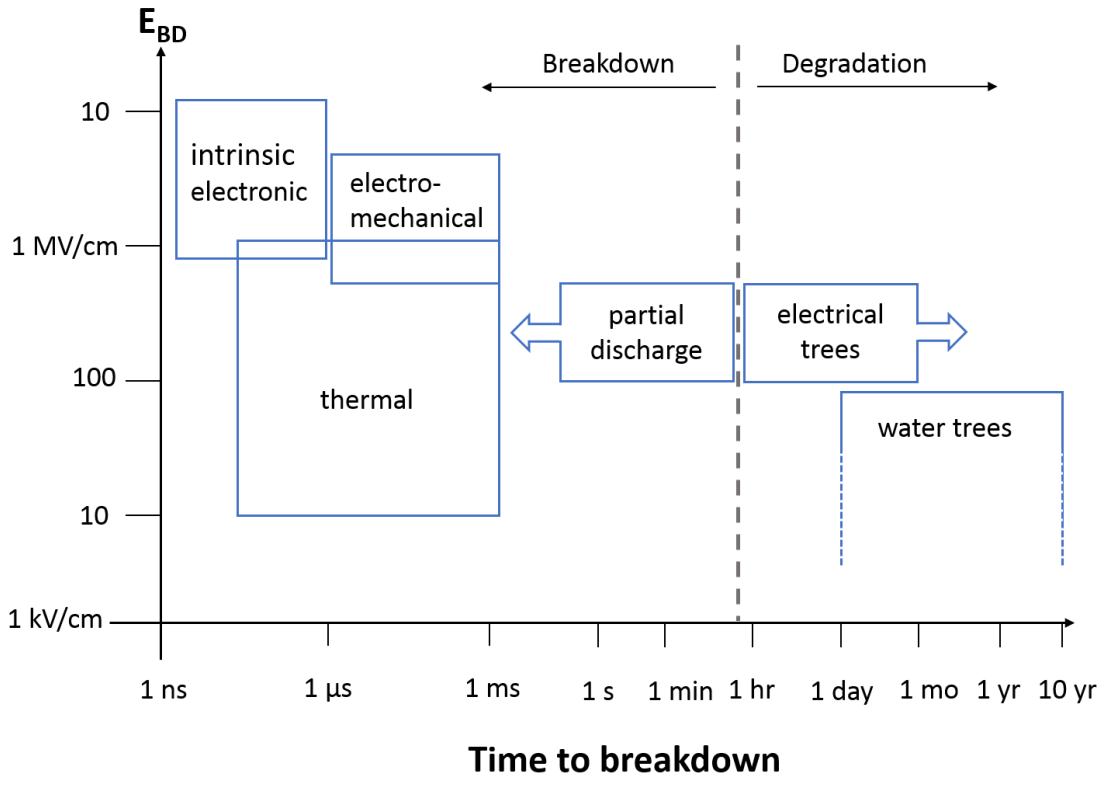

Figure 2-9: Times and electric fields at which various electrical breakdown mechanisms are operative. No clear distinction between breakdown and degradation [23].

2.3.5.1 Electrical breakdown

2.3.4.2 Thermal Breakdown

Under the applied electric field, the dielectric generates heat due to conductance and dielectric loss thus increasing its temperature, and the conductance and loss increase with elevated

temperature, further causing the temperature to rise. A schematic process of heat versus temperature for different voltages ($V_1<V_2<V_3$) in shown in **Figure 2-10b** [25]. The heat loss obeys the Newton cooling law and is denoted as a straight line, and the three curved lines indicate the heat generated under different voltages. When $V= V_1$, the heat generated and heat loss intercept at $T= T_1$, indicating a heat balance has been created. A small increase in T would lead to the heat loss higher than heat generated thus temperature would drop back to T_1 and vice versa. When $V= V_2$, a metastable balance has been created at T_2, any rise on the temperature would lead to the heat generated higher than the loss thus causes a thermal runaway, in this case the heat balance in the material is broken, the temperature rises continuously, and eventually thermal damage occurs, i.e., thermal breakdown occurs. The voltage V_2 is the maximum voltage attainable with respect to thermal breakdown, because no higher voltage (V_3) would create the heat balance and would inevitably cause the thermal runaway. Thermal breakdown is not only related to the nature of the dielectric material itself, but also to the type and frequency of the applied voltage, ambient temperature, heat dissipation conditions, etc.

2.3.4.3 Electromechanical Breakdown

Electromechanical breakdown occurs when the mechanical compressive stress on the dielectric caused by the electrostatic attraction of the electrodes exceeds a critical value which cannot be balanced by the elasticity of the dielectric (as shown in **Figure 2-10c**). The electromechanical breakdown voltage can be evaluated by equating these two stresses for the equilibrium situation before breakdown in a parallel-plate dielectric slab:

$$\frac{\varepsilon_0 \varepsilon_r}{2}\left(\frac{V}{d}\right)^2 = Y \log\left(\frac{d_0}{d}\right) \qquad \textbf{2-19}$$

thus

$$E_c = \frac{V_c}{d} = \left(\frac{Y}{\varepsilon_0 \varepsilon_r}\right)^{\frac{1}{2}} \quad \textbf{2-20}$$

where E_c is the characteristic breakdown strength, V is the applied Voltage, Y is the Young's modulus of elasticity, d_0 is the initial dielectric thickness and d is the reduced dielectric thickness after applied V. Low Y material like polymer is more likely to endure electromechanical breakdown [23].

2.3.4.4 Partial Discharge Breakdown

Many solid dielectrics have their own intrinsic breakdown field strength, but the actual measured breakdown strength tends to be lower than predicted, sometimes even one to two orders of magnitude. One of the important reasons for this phenomenon is partial discharge.

In practical measurements, there are often impurities such as bubbles and droplets in the dielectric material, and the breakdown strength of gases and liquids is low. Therefore, when the applied electric field increases to a certain value, the breakdown begins to start from these weak areas and appears as local. Discharge then develops over time, leading to a complete breakdown of the dielectric as shown in **Figure 2-10d** [24].

2.3.4.5 Probability distributions for failure: two-parameter Weibull Statistical

It should be noted that, in practical applications, the geometrical dimensions of the

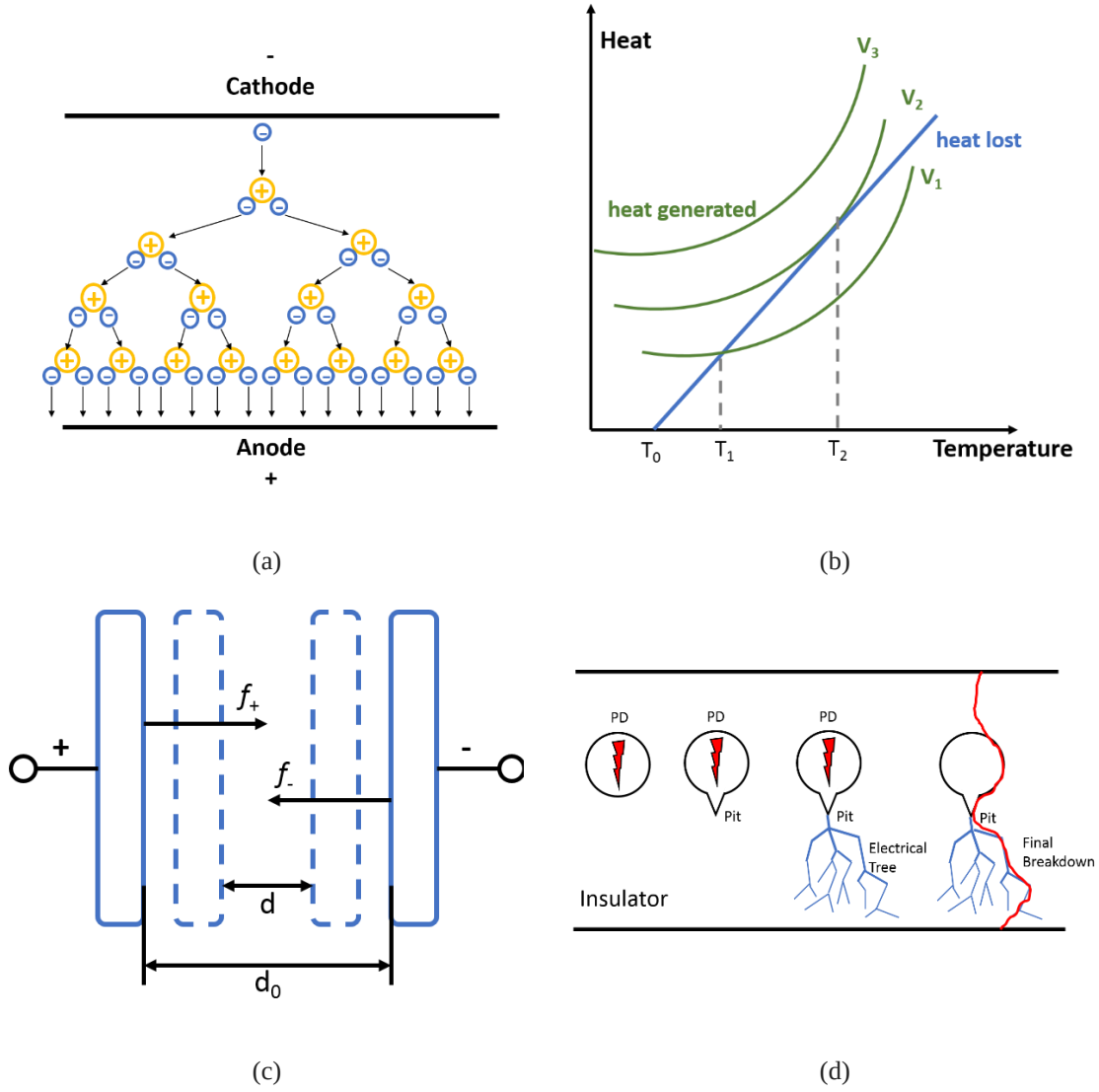

Figure 2-10: Schematic figure of typical breakdown mechanism. (a) electrical breakdown; (b) thermal breakdown; (c) electromechanical breakdown and (d) partial discharge breakdown [24].

dielectric material is generally large, and the chemical composition and the material structure are inevitably uneven, resulting in a large numerical dispersion of the breakdown strength. According to this situation, the researchers developed a defect theory that is applicable to the actual material breakdown law: the material contains defects (holes, impurities or thin areas etc.), these defects sustain the most concentrated electric field, resulting in the failure of the overall material. From a

statistical point of view, the occurrence of defect is a random event, so the breakdown field strength restricted by the distribution of the vulnerability is also a random event, so its law can be processed by statistical methods like Weibull statistics. Usually, the breakdown field strength is only a statistic value [21, 26-29].

The key to statistics breakdown data analysis is to fit the collected test data to a probability distribution function distribution according to a certain distribution model. With the probability density function, it is easy to get the reliability and cumulative failure probability. Among them, the Weibull distribution is the most popular distribution in characterizing times to failure for solid insulation. Under constant DC or AC voltage conditions as in this study, the probability of failure can be described by the two-parameter Weibull distribution, its probability density function is written as:

$$f(t) = \frac{\beta}{\alpha}(\frac{t}{\alpha})^{\beta-1}e^{-(\frac{t}{\alpha})^{\beta}} \quad \textbf{2-21}$$

Where β is the shape factor, α is the characteristic life at which 63.2% failure occurs.

The equation of Weibull distribution or the cumulative distribution function is written as:

$$F(t) = \int_0^t f(t)dt \ = 1 - e^{-\left(\frac{t}{\alpha}\right)^{\beta}} \quad \textbf{2-22}$$

Thus, the reliability function (or survivor function) at time t, which is the probability of not failing by time t, is defined as:

$$R(t) = 1 - F(t) = \int_t^{\infty} f(t)dt \ = e^{-(\frac{t}{\alpha})^{\beta}} \quad \textbf{2-23}$$

Take second logarithm on both sides of the **equation 2-23**, so that the equation with exponent can be changed into a linear equation:

$$ln(1 - F(t)) = ln(e^{-\left(\frac{t}{\alpha}\right)^{\beta}}) \quad \textbf{2-24}$$

and

$$ln(ln(1 - F(\mathrm{t}))) = \beta\ln(\frac{t}{\alpha}) \quad \textbf{2-25}$$

Set

$$y = ln(ln(\frac{1}{1-F(t)})) \quad \textbf{2-26}$$

and

$$x = ln(t) \quad \textbf{2-27}$$

Then

$$y = \beta \cdot x - \beta \cdot ln(\alpha) \quad \textbf{2-28}$$

The **equation 2-28** represents a straight line in the form of "y= ax + b" as shown in the Weibull cumulative distribution function (CDF) plot in **Figure 2-11a**. The slope of this line is the shape parameter β in the Weibull function, and the time point on the x-axis corresponding to P_F (α_c) = 1-(1/e) = 63.2% of the y-axis is the characteristic scale parameter α_c or in this case characteristic breakdown strength (E_{BD}) [23, 30, 31].

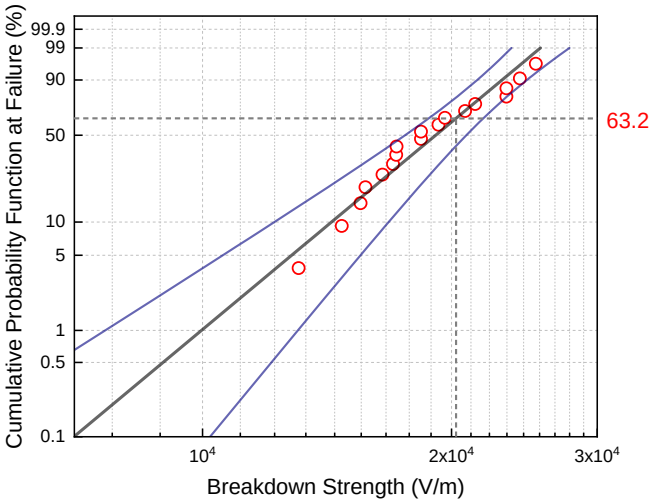

(a)

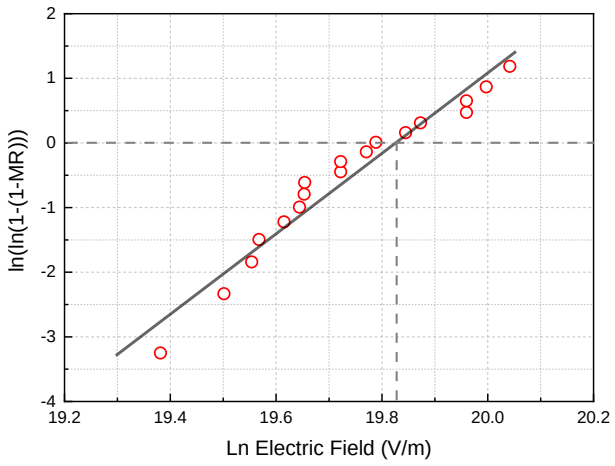

(b)

Figure 2-11: Weibull statistic of breakdown. (a) CDF plot. The horizontal dashed line is the 63.2% quantile and its intercept with the fitting line indicates the scale parameter α - characteristic breakdown strength (E_{BD}). The slope of the fitted line indicates the shape parameter β. The curved lines bracketing the data represent 95% confidence limits. (b) Weibull plot of sample data using median rank method and fitted regression line.

A regression routine has been employed to remove the element of subjectivity, among them, the median rank method is an excellent numerical approximation. The median rank is defined as:

$$MR = \frac{j - 0.3}{N + 0.4} \qquad \textbf{2-29}$$

Where j is the rank and N is the total number of data points. After all data points are sorted in ascending sequence, plot the data in the ln Electric Field vs. ln(ln(1/(1-MR))) plot as shown in **Figure 2-11b**. A least square method is utilized to get the straight fitting line. The intercept with the x axis of the fitted line indicates the characteristic breakdown strength and the slope indicates the shape parameter β. In this study, the lowest value β is characterized as the failure tolerance. A more detailed investigation of how the shape parameter β reflect the distribution of the failure data is shown in **Figure 2-12** with same scale parameter α (α = 1) but different shape parameter β (β= 0.5,1.0, 1.5, 2.0, 3.0). The time scale has been normalized to time/ (characteristic time) so that a normalized time equal to one indicates a time equal to the characteristic time to breakdown. The cumulative probability of failure plot (**Figure 2-12a**) indicates the failure probability at time t.

When t increases, the probability at failure increases until it eventually approaches unity (certain failure). Higher β value leads to an earlier approach to certain failure. It is more obvious in the probability density function plotted in **Figure 2-12b** why β is known the shape parameter. With increasing β value, the shape of the function peaked for β > 1, and higher β value indicates a narrower distribution of failure time.

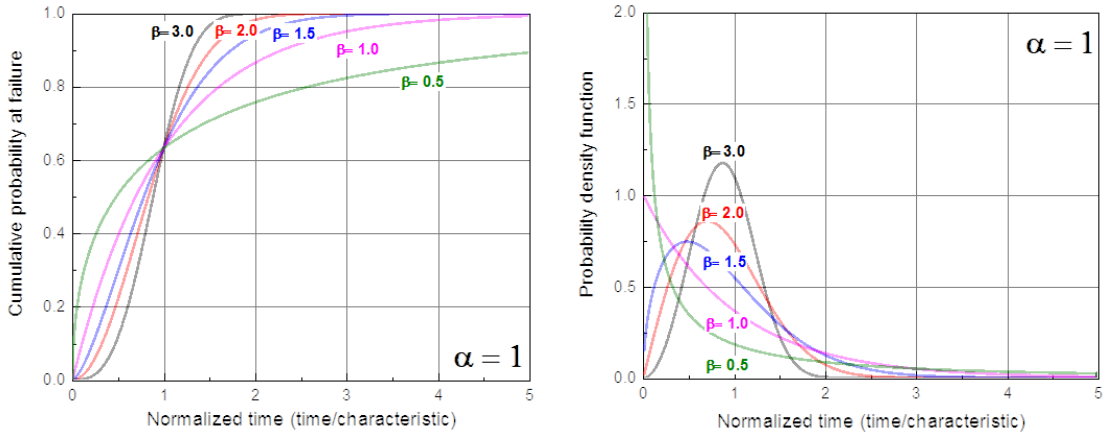

(a) (b)

Figure 2-12: **(**a) The cumulative probability of failure function $P_F(t)$ and (b) the probability density function f(t) of the Weibull distribution for the five cases of α= 1, β= 0.5,1.0, 1.5, 2.0, 3.0 [32].

2.3.6 Polarization - Electric Field Loop (P-E loop)

Polarization- electric field loop is the variation of electric polarization (C/m^2) with electric field (V/m). It is a method to calculate the energy storage and energy loss in both linear and non-linear materials. The dielectric displacement ($D \equiv \varepsilon_0 E + P$) is the sum of the material and vacuum contributions to induced charge Q [32].

Under a sine wave AC voltage $V = V_0 sin(\omega t)$, the charge induced for an ideal linear dielectric material Q_C is:

$$Q_C = \int I\,dt = \int C\frac{dV}{dt}\cdot dt = \int C\,dV = C\cdot V_0 sin(\omega t) \qquad \textbf{2-30}$$

as shown in **Figure 2-13a**, which is a straight line with a gradient of capacitance C.

And the charge induced for an ideal resistor Q_R is:

$$Q_R = \int I\,dt = \int \frac{V}{R}\,dt = \frac{1}{R}\int_0^+ V_0 sin(\omega t)dt = \frac{V_0}{\omega R}(1 - cos(\omega t)) \quad \textbf{2-31}$$

as shown in **Figure 2-13b**, which is an ellipse with the bottom at the origin.

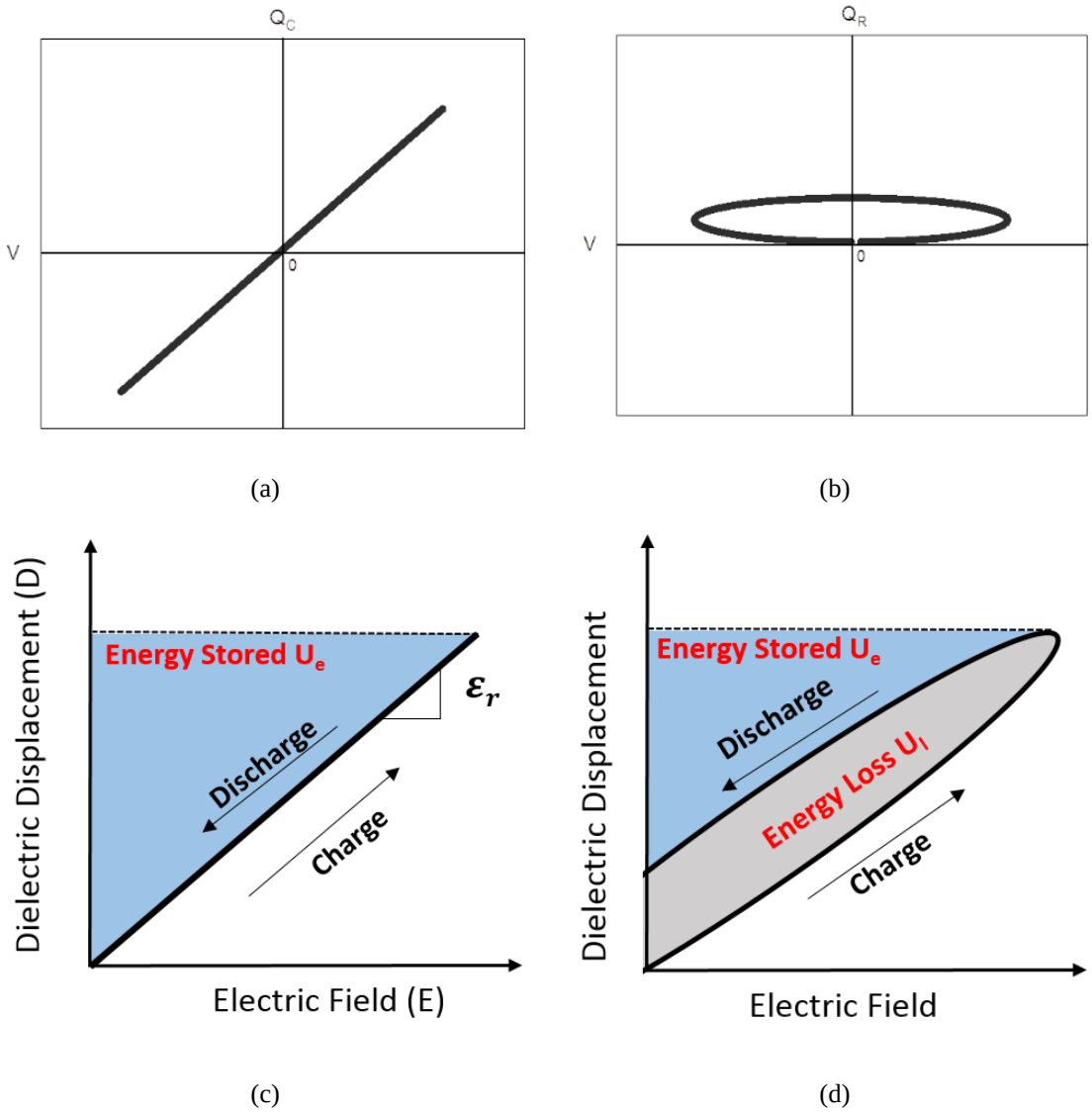

Figure 2-13: Schematic charge- voltage plot of (a) ideal linear capacitor and (b) ideal resistor response; Schematic displacement- electric field plot (c) ideal linear capacitor and (d) lossy linear capacitor.

When the charge and voltage are normalized by the sample dimensions, the electric displacement- electric field plot is achieved as shown in **Figure 2-13c**, whose energy density stored (recoverable) $U_e = \int EdD$ is shown in the shaded area and its gradient is proportional to the

relative permittivity ε_r [33]. In practical applications, the linear dielectric material can be considered as an ideal capacitor and an ideal resistor in parallel, as discussed in **section 2.3.3**, thus the representative P-E loop of a lossy linear dielectric is a combination of **Figure 2-13a** and **Figure 2-13b**, resulted in **Figure 2-13d**. Inside the charge-discharge cycle is the energy density loss U_l during the process, and the energy efficiency $\eta = U_e/(U_e + U_l)$

2.4 References

1. Smallwood, I., Handbook of organic solvent properties. 2012: Butterworth-Heinemann.

2. Licari, J.J. and L.A. Hughes, Handbook of polymer coatings for electronics: chemistry, technology and applications. 1990: William Andrew.

3. Grosso, D., How to exploit the full potential of the dip-coating process to better control film formation. *Journal of Materials Chemistry*, 2011. **21**(43): p. 17033-17038.

4. Scriven, L. Physics and applications of dip coating and spin coating. in MRS Proceedings. 1988. Cambridge Univ Press.

5. Xia, S., G. Liu, and V. Birss, Properties of thin polystyrene films prepared on gold electrodes by the dip-coating method. *Langmuir*, 2000. **16**(3): p. 1379-1387.

6. Schwartz, L. and L. White, Modelling of the dip-coating process. 1994.

7. Schneller, T., et al., Chemical solution deposition of functional oxide thin films. 2013, Springer.

8. Jiang, J., et al., Surface Characteristics of a Self-Polymerized Dopamine Coating Deposited on Hydrophobic Polymer Films. *Langmuir*, 2011. **27**(23): p. 14180-14187.

9. Weldon, D.G., Failure analysis of paints and coatings. 2009: John Wiley & Sons.

10. Kauffman, G.W. and P.C. Jurs, Prediction of Surface Tension, Viscosity, and Thermal Conductivity for Common Organic Solvents Using Quantitative Structure−Property Relationships. *Journal of Chemical Information and Computer Sciences*, 2001. **41**(2): p. 408-418.

11. Macdonald, J.R., Impedance Spectroscopy: Theory, Experiment, and Applications, ed. 2. 2005.

12. Kao, K.C., Dielectric phenomena in solids. 2004.

13. Bräunlich, P., Thermally stimulated relaxation in solids. Thermally stimulated relaxation in solids, 1979. **1**.

14. Neagu, E.R. and R.M. Neagu, On the nature of the origin of the isothermal and non-isothermal current released from dielectric materials. *Thin Solid Films*, 2001. **384**(1): p. 15-22.

15. Van Turnhout, J., Thermally stimulated discharge of polymer electrets. *Polymer Journal*, 1971. **2**(2): p. 173-191.

16. van Turnhout, J., Thermally stimulated discharge of electrets. 1980. **33**: p. 81-215.

17. Bucci, C., R. Fieschi, and G. Guidi, Ionic Thermocurrents in Dielectrics. *Physical Review*, 1966. **148**(2): p. 816-823.

18. Hong, C.-M. and D.E. Day, Thermally stimulated polarization and depolarization current (TSPC/TSDC) techniques for studying ion motion in glass. *Journal of Materials Science*, 1979. **14**(10): p. 2493.

19. Hong, C.-M. and D.E. Day, Thermally Stimulated Currents in Sodium Silicate Glasses. *Journal of the American Ceramic Society*, 1981. **64**(2): p. 61-68.

20. Dash, P., et al., High electric field conduction in low-alkali boroaluminosilicate glass. *Journal of Applied Physics*, 2018. **123**(5): p. 054102.

21. Klein, N., Electrical breakdown in thin dielectric films. *Journal of the Electrochemical Society*, 1969. **116**(7): p. 963-972.

22. Bluhm, H., Pulsed Power Systems. 2006.

23. Dissado, L.A. and J.C. Fothergill, Electrical degradation and breakdown in polymers. 1992: IET.

24. Painter, P.C. and M.M. Coleman, Essentials of polymer science and engineering. 2008: DEStech Publications, Inc.

25. Harari, E., Dielectric breakdown in electrically stressed thin films of thermal SiO2. *Journal of Applied Physics*, 1978. **49**(4): p. 2478.

26. Hyun Choi, D., C. Randall, and M. Lanagan, Combined electronic and thermal breakdown Models for polyethylene and polymer laminates. *Materials Letters*, 2015. **141**: p. 14-19.

27. Lee, H. and M.T. Lanagan, Dielectric-breakdown and conduction-mechanism in a thinned alkali-free glass. *Journal of the Korean Physical Society*, 2014. **65**(7): p. 955-959.

28. Murata, T., et al., Electrode-Limited Dielectric Breakdown of Alkali Free Glass. *Journal of the American Ceramic Society*, 2012. **95**(6): p. 1915-1919.

29. Ridley, B.K., Mechanism of electrical breakdown in SiO2films. Journal of Applied Physics, 1975. **46**(3): p. 998-1007.

30. Murthy, D.P., M. Xie, and R. Jiang, Weibull models. Vol. 505. 2004: John Wiley & Sons.

31. McCool, J.I., Using the Weibull distribution: reliability, modeling, and inference. Vol. 950. 2012: John Wiley & Sons.

32. Kasap, S.O., Principles of electronic materials and devices. Vol. 81. 2006: McGraw-Hill New York, NY.

33. Palneedi, H., et al., High-performance dielectric ceramic films for energy storage capacitors: progress and outlook. *Advanced Functional Materials*, 2018. **28**(42): p. 1803665.

Chapter 3
Low Electric Field Properties

3.1 Introduction

This chapter describes the experimental procedures used to characterize the low electric field properties of the glass and glass-polymer laminates. In **section 3.2** the dielectric permittivity and loss properties of both the glass and polymer-glass laminate were measured by dielectric relaxation spectroscopy, and two types of low-alkali glass (AF45 and OA-10G) properties were compared. Impedance spectroscopy has been frequently used in the past to determine activation energy for ionic conduction, relaxation frequency for ionic hopping and thickness of depletion layer in thermoelectrically poled glasses [1-6]. In the **section 3.3**, the complex impedance plots (Nyquist Plot) of the thermally poled OA-10G glass were studied using equivalent circuit model and the thickness of the glass depletion layer was calculated though its fitted capacitance.

3.2 Dielectric Relaxation Spectroscopy

The energy storage density (U_e) is a comprehensive factor reflecting the amount of electrical energy stored in the dielectric material. The higher the energy storage density, the better the performance of storing electrical energy. The calculation formula of the energy storage density is as follows:

$$U_e = \int_0^D E \, dD \qquad \textbf{3-1}$$

Where, the U_e is the storage energy density of the dielectric, E is the breakdown strength, and D is the electrical displacement. For linear dielectric materials (polarization is proportional to the electric field), the calculation equation for the energy storage density can be abbreviated as:

$$U_e = \frac{1}{2}\varepsilon_0\ \varepsilon_r E^2 \quad \textbf{3-2}$$

Usually the actual working field of the dielectric material is lower than its breakdown strength, so an effective way to increase the energy storage density of the dielectric material is to increase its dielectric constant.

Dielectric loss (tanδ) refers to the consumption of a dielectric material that converts a portion of the electrical energy into thermal energy due to changes in the direction of the electric field under an alternating flow electric field. According to the mechanism, dielectric loss can be divided into conductance loss and polarization loss. Conductance loss refers to the loss of energy caused by carriers in a dielectric material under the electric field and leakage current. At low frequencies, the dielectric loss of the dielectric is dominated by conductance losses. Polarization loss means that under the applied electric field, the orientation polarization of the dielectric material is not able to keep up with the change of the frequency, and the energy loss caused by overcoming the internal resistance. Usually the polarization loss is related to the frequency of the electric field. At lower frequencies, the dielectric material has enough response time to the frequency and therefore has little polarization loss. As the frequency increases, the dielectric material lags the electric field, causing a large energy loss. In the relationship between dielectric loss and frequency, the dielectric loss decreases first and then increases as the frequency increases [7-9].

The dielectric constant and dielectric loss can maintain their temperature independence up to 250 °C; after that, a space charge polarization is triggered, increasing the dielectric loss in both glasses. It is known that in the AF45 glass, Na^+ ions and Ba^{2+} ions can be delocalized from their tapping sites, contributing to the observed depolarization current peaks [10-12]. Other ions are still trapped in the deeper energy states and cannot be easily activated. Here it is assumed that the same

detrapping process occurs in the OA10G glass. Given that the conductivity follows $\sigma = \mu nq$ (where μ is the mobility of the carriers with the charge of q, and n is the concentration of carriers), Since Na^+ ions have smaller activation energy and show a current peak at a lower temperature than Ba^{2+} ions, Na^+ ions are the first mobile ions liberated from their frozen states at intermediate temperatures. The initially measured ratio is not commensurate with the Na^+ mole ratio between the two glasses (**Table 3-1**), because the activation of Na^+ ions is a thermally activated process, during which different fractions of Na^+ ions are gradually mobilized in the two glasses; with increasing temperature, the conductivity ratio continues to grow closer to the Na^+ mole ratio. The dielectric loss of AF45 is four times greater than OA10 G at 400 ^oC (**Figure 3-1**), which is commensurate with the sodium ratio shown in **Table 3-1**.

Table 3-1: Compositions of the two glasses: AF45 and OA10G

mol %	SiO_2	B_2O_3	Al_2O_3	MgO	CaO	SrO	BaO	As_2O_3	SnO_2	Na_2O
AF45	63.6	15.0	9.1	N/A	N/A	.163	11.9	.33	.0007	.074
OA10G	66.7	9.2	10.7	.5	9.6	3.0	.2	N/A	.101	.018
ion ratio (AF45/OA10G)	.95	1.63	.85	N/A	N/A	.05	59.5	N/A	.007	4.11

As shown in **Figure 3-2**, both glass and laminate show a stable dielectric constant and loss over a wide frequency range at room temperature; no relaxation or charge motion can be identified as the temperature is far below the glass transition temperature of both components. As temperature increases to 300 °C, a limited charge movement is observed, as evidenced by the increase of both

dielectric constant and dielectric loss, a typical behavior of space-charge polarization, or Maxwell-Wagner-Sillars (MWS) polarization. But it remains uncertain:

1.Whether a long-range quasi-DC conductivity is superimposed on the space-charge polarization

2.Whether there exists additional contribution from the trapped charges on the polymer-glass interface to the observed MWS polarization.

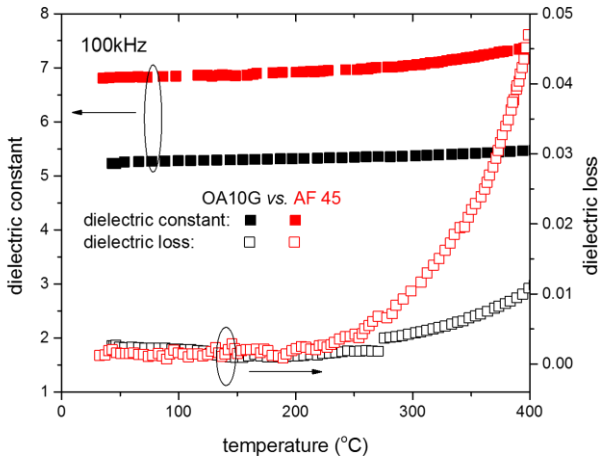

Figure 3-1: Dielectric spectrum of OA10G vs. AF45 at 100 kHz (the specific formulations of the two glasses are summarized in **Table 3-1**)

As the coated polymer is substantially thinner than the glass, the contribution of the polymer coating to the total series capacitance is also lower. The impedance of the glass-glass polymer laminate is dominated by the glass, therefore the influence of the polymer coating on the low-field permittivity cannot be observed. Considering the energy density of a material is proportional to its permittivity as in **equation 3-2**, the energy density of the glass is not diluted by the polymer coating thus has no adverse impact on the proposed polymer-glass laminate material.

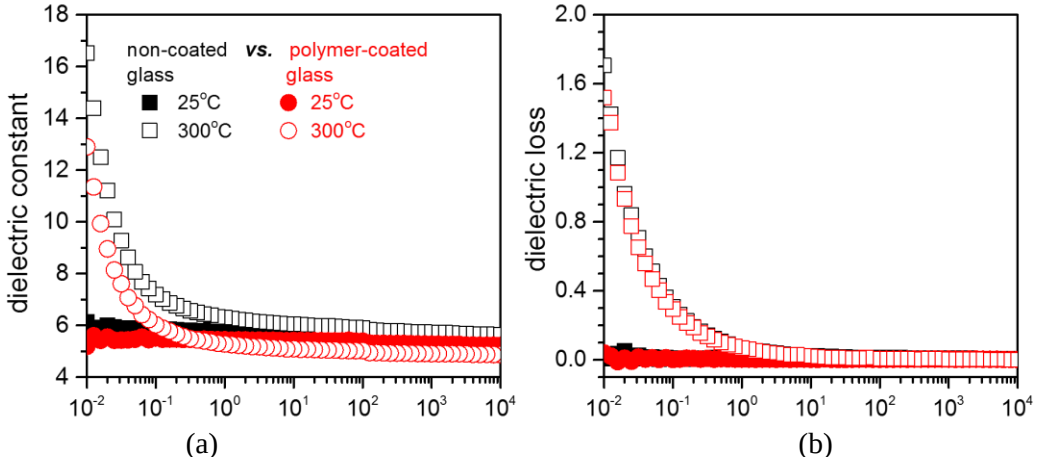

Figure 3-2: (a) Dielectric spectroscopy for the glass (OA10G) and the laminate (FPE-OA10G) at 25 °C and 300 °C; (b) the dielectric properties of the glass dominate the laminate dielectric properties.

3.3 Impedance Spectroscopy

The complex capacitance measurements of a poled (500V, 300ºC-500°C, 3 hours) 20 μm OA-10G glass (D=10mm, 100nm Al electrode) were conducted using ModuLab (XM MTS, Solartron Analytical, Hampshire, UK) over a frequency range of 10^{-2} – 10^{6} Hz, temperature range of 300°C to 500°C with an applied 1V AC voltage. The configuration of the ModuLab is shown in **Figure 3-3**. An input is applied to the amplifier A1 such that the output is the required waveform. This passes through a resistor for cable matching and is applied to the sample as the generated voltage (GEN). The resulting potential difference across the sample (V_{hi}, V_{lo}) is passed through amplifier A2 to the voltage measurement circuit. The output current (I) is passed through the amplifier A3 which produces a voltage for measurement purposes, proportional to the current. Before conducting any impedance measurements, a calibration was carried out using an internal reference calibration. This includes the calibration of the reference capacitors relative to each other and additional internal components used in the reference measurement mode [13].

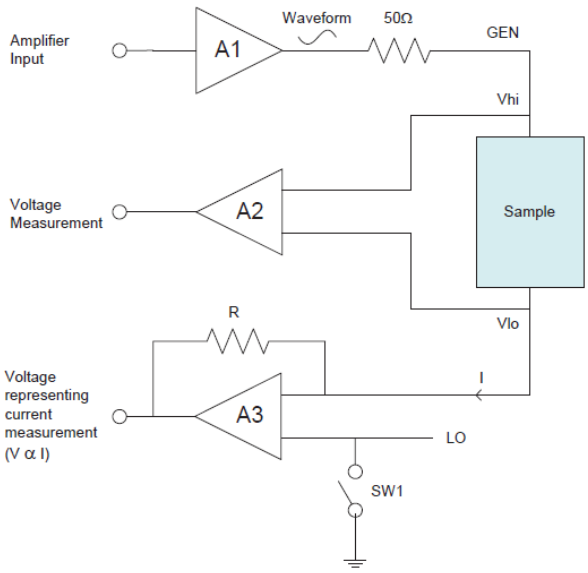

Figure 3-3: Waveform generation and measurement [14].

For instance, theoretically, a perfect capacitor does not generate any energy loss by itself, however, since the material used to make the capacitor has resistance, the capacitor becomes imperfect. This loss is external, and it could be represented as a resistor connected in parallel with the capacitor. As shown in **Figure 3-4**, the electrical property of the polymer coated glass could be studied by using an equivalent circuit – each layer is represented by a resistor and capacitor in parallel, and three of them in series composes of the sandwiched sample structure.

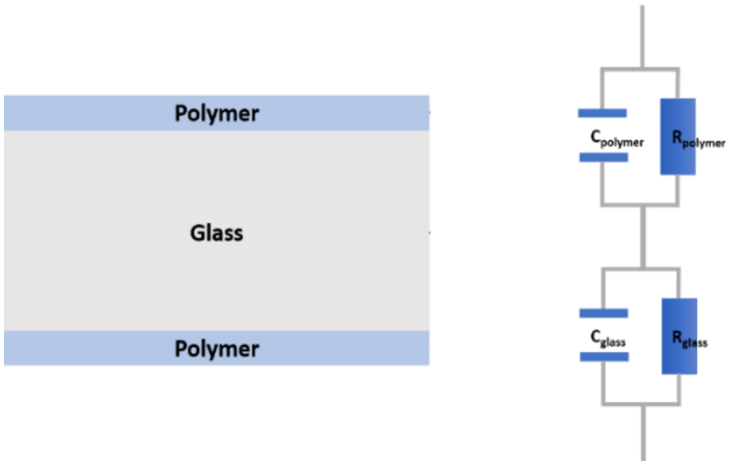

Figure 3-4: Equivalent circuit model of a polymer coated glass sample

For the practical IS measurement, two examples of poled glass results are shown in **Figure 3-5**. In the case of poled soda lime glass **Figure 3-5a**, the double 'semicircles' deviate from its ideal model as in **Figure 3-5d** and appeared to be circular arcs. This phenomenon is attributed to the distributions of time constant (τ= RC) which commonly exist in inhomogeneous systems and leads to the suppressions of the arcs below the real plane of Nyquist plot [7]. In another poled glass (low-alkali boroaluminosilicate glass AF45) example in **Figure 3-5b**, the first semicircle does not meet the x axis at (R1, 0) is attributed to the same phenomenon but less time constant distributions. Neither of the Nyquist plot shows the entire second semicircle on the right due to the instrument limit of the frequency range (0.01Hz).

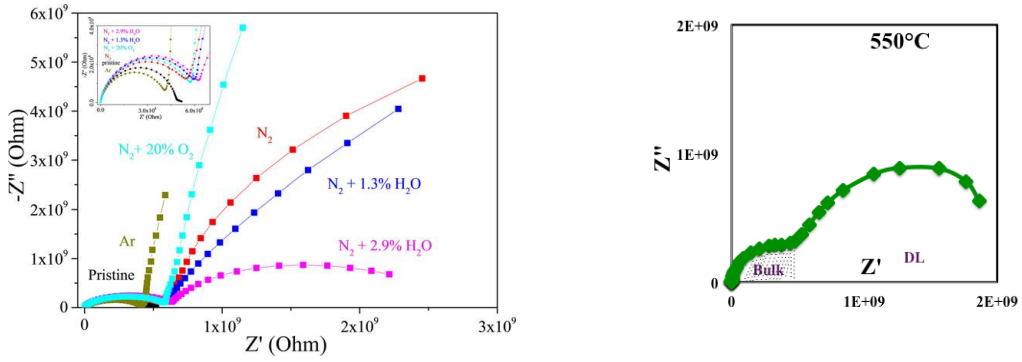

(a) (b)

Figure 3-5: Nyquist Plot with double semicircles of poled glass sample. (a) soda lime silica (SLS) glass [15] (b)Low-alkali Boroaluminosilicate AF45 glass [16].

A Nyquist plot of the FPE coated 50 μm AF45 glass and uncoated AF45 glass under 1V, 300ºC is shown in **Figure 3-6a**. Even at high temperature, due to the low conductivity (high resistivity) of the low-alkali glass, the polymer layer cannot be distinguished from the glass layer (which would appear as a second semicircle on the lower end of the impedance axis).

Figure 3-6bc shows the Nyquist plot of the thermally poled 20μm OA-10G to calculate the individual values of resistance and capacitance of two regions formed during thermal poling using

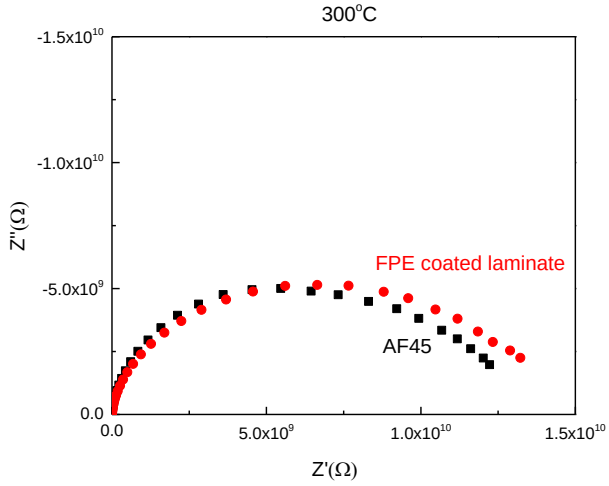

(a)

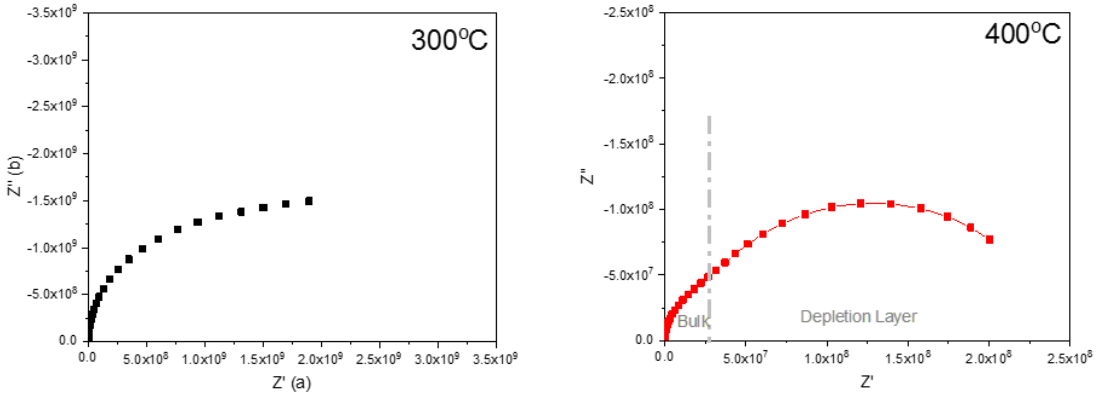

(b) (c)

Figure 3-6: Nyquist plots for (a) 50µm AF45 glass and FPE coated AF45 glass-polymer laminate, poled 20µm OA-10G glass for 3hrs, 500V at (a) 300°C and (b) 400°C

the equivalent circuit model [1]. The resistance could then be denoted as R_B (bulk glass) and R_{DL} (depletion layer) respectively, and capacitance as C_B and C_{DL}. The depletion layer thickness (d) could then be calculated using equation:

$$d = \frac{\varepsilon_0 \varepsilon_r A}{C_{DL}} \quad \textbf{3-3}$$

where, ε_0, ε_r, A and C_{DL} are the absolute permittivity, relative permittivity, electrode area and calculated capacitance of the depletion layer. It is assumed that the relative permittivity of the depletion layer is the same as the bulk glass (as received glass) [16].

At lower temperature (below 300ºC), both the impedance and time constant τ= RC of the depletion layer are extremely large (higher than the instrument limit $10^{12}\Omega$), thus only at high temperatures (above 400°C) the two impedance semicircles can be separated. The capacitance C_{DL} obtained by fitting the complex impedance data at 400°C is 4.23×10^{-10} F that provides a depletion layer thickness of 8.2 μm using **equation 3-3Error! Reference source not found..**

3.4 Conclusions

The low electrical field dielectric properties of the glass and polymer-glass laminates are studied by using dielectric relaxation spectroscopy (DRS) and impedance spectroscopy (IS). The permittivity and loss of the two low-alkali glass is associated with their own sodium content. Considering the large impedance of the glass, the low electrical field property of the polymer-glass laminate is dominated by the glass, thus the laminate maintains the same energy density as the glass (the polymer contribution could be neglected). The impedance response from the thermally poled glass was fitted with an equivalent circuit combined of two resistor and capacitor in parallel, and these two parts represent the glass depletion layer and the bulk glass. Though the Nyquist plot of the IS, two impedance semicircles can be fitted using Z-View software and the depletion layer thickness could thus be calculated. It critical information from the low electric field property is that the permittivity of the polymer- glass laminate does not change after a thin layer polymer coating, and based on the energy density equation $U_e = \frac{1}{2} \varepsilon_o \varepsilon_r E_{BD}^2$ this indicates the high energy density achieved by the low-alkali boroaluminosilicate glass would not be influenced by the laminate

structure. This has also been confirmed from the relative permittivity calculated from the high electric field P-E loop results in **section 4.3**.

3.5 References

1. Lepienski, C., et al., Electric field distribution and near-surface modifications in soda-lime glass submitted to a dc potential. *Journal of non-crystalline solids*, 1993. **159**(3): p. 204-212.

2. Cordaro, J. and M. Tomozawa, Dielectric Relaxation Strength of a Low‐Alkali Glass. *Journal of the American Ceramic Society*, 1981. **64**(12): p. 713-717.

3. Maia, L.F. and A.C. Rodrigues, Electrical conductivity and relaxation frequency of lithium borosilicate glasses. *Solid State Ionics*, 2004. **168**(1-2): p. 87-92.

4. Doi, A., Simulation and scaling of ac conductivities in ion-conducting glasses. *Journal of non-crystalline solids*, 2006. **352**(8): p. 777-782.

5. Dutta, A., et al., Ac conductivity and dielectric relaxation in ionically conducting soda–lime–silicate glasses. *Journal of non-crystalline solids*, 2008. **354**(33): p. 3952-3957.

6. Tomozawa, M. and R. Doremus, Experimental measurements of dielectric relaxation in glass. *Journal of non-crystalline solids*, 1974. **14**(1): p. 54-64.

7. Jonscher, A.K., Dielectric Relaxation in Solids. 1983: Chelsea Dielectrics Press.

8. Kasap, S.O., Principles of electronic materials and devices. Vol. 81. 2006: McGraw-Hill New York, NY.

9. Kao, K.C., Dielectric phenomena in solids. 2004.

10. Smith, N.J., Novel approaches to the surface modification of glass by thermo-electric poling. 2011, The Pennsylvania State University.

11. Carlson, D., Ion depletion of glass at a blocking anode: I, theory and experimental results for alkali silicate glasses. *Journal of the American Ceramic Society*, 1974. **57**(7): p. 291-294.

12. Kudlinski, A., et al., Complete characterization of the nonlinear spatial distribution induced in poled silica glass with a submicron resolution. *Applied Physics Letters*, 2003. **83**(17): p. 3623-3625.

13. Liu, W.-E., Impedance/thermally stimulated depolarization current and microstructural relations at interfaces in degraded perovskite dielectrics. 2009, The Pennsylvania State University.

14. Modulab User Guide.

15. Luo, J., et al., Chemical structure and mechanical properties of soda lime silica glass surfaces treated by thermal poling in inert and reactive ambient gases. *Journal of the American Ceramic Society*, 2018. **101**(7): p. 2951-2964.

16. Dash, P., Dynamics of Space Charge Polarization and Electrical Conduction in Low Alkali Boroaluminosilicate Glasses. 2013.

Chapter 4

High Electric Field Properties

4.1 Introduction

This chapter summarizes the dielectric properties of the low-alkali boroaluminosilicate glass and polymer coated laminate under high electric field. As mentioned in **section 2.3.5**, the breakdown strength of the dielectric is a vital characteristic for energy density, thus it is important to study the ion movement under high electric field as a precursor to dielectric failure. In **section 4.2**, the Thermally Stimulated Depolarization Current (TSDC) measurement is employed to study the conduction mechanism. Movement of ionic and electronic charge has a significant effect on the local electric field distribution with glass. Electric Polarization- Electric Field loop (P-E loop) is adopted in **section 4.3** to verify the permittivity change under high electric field. Dielectric breakdown test at room temperature, elevated temperature (**section 0**) and after thermal poling (using Highly Accelerated Life Testing system, **section 4.5**) are done to understand the breakdown mechanism of the proposed glass and polymer-glass laminate. In **section 4.6**, different polymer coating has been investigated to show the benefit of the laminate structure.

4.2 Thermally Stimulated Depolarization Current (TSDC)

Figure 4-1 shows a representative example of high-field TSDC measurement for low-alkali glass AF45 [1]. The 50 μm AF45 sample with 50 nm thick and an area of 0.785 cm^2 Pt electrode is poled at room temperature under an electric field of 3 MV/cm with a ramp rate of 10 V/s and then heated from room temperature to 450 ^oC to obtain the depolarization current. The peak

P_2 at around 225 °C and P_3 at 400 °C has been confirmed to originate from Na^+ and Ba^{2+} separately by calculating its activation energy. Their current flow is in the opposite direction as during cooling under the polarization field. However, P_1 at around 70 °C shown in shaded area indicates that the current is flowing in the same direction as the polarization field. It has been elucidated that this is due to the had ionic and electronic contributions. The electrons are transported in the glass through field-assisted lowering of the potential barrier of trapped electrons in the bulk insulator, namely Poole-Frenkel emission [1].

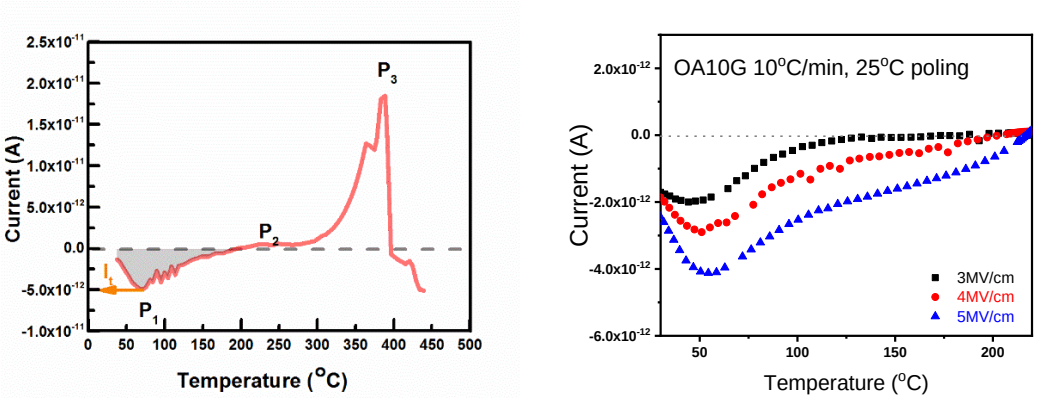

(a) (b)

Figure 4-1: (a) High field TSDC in 50 µm AF45 glass poled at 25°C under an electric field of $3*10^8$ V/m showing evidence of electronic conduction (shaded area). Ramp rate used was 10 V/s. The peak current I_t for the electron relaxation current was used to fit the IV data to different electronic conduction models. P_1, P_2, and P_3 denote relaxation current due to electrons, Na^+ and Ba^{2+} ions respectively [1]. (b) High field TSDC in 10 µm OA1OG poled at 25 °C under an electric field of 3,4 and 5 MV/cm confirming the existence of the hetero charge.

In order to confirm this phenomenon, another low-alkali glass OA10G sample is tested using similar method. 100nm Pt electrode is sputtered on both sides of the 10µm OA10G sample with a diameter of 10mm to achieve more signal. The OA10G sample is heated from 25 °C to a polarization temperature of 250 °C, and then a DC high voltage electric field is applied to the sample. The polarization field strengths used in the test are 3, 4, 5 MV / cm, respectively, and the polarization time is 20 minutes (to meet the requirements for equilibrium polarization of the sample), the polarization field strength remains unchanged, and the sample temperature is rapidly

cooled back to 25 °C. At this time, the dipole orientation alignment in the sample is frozen, and the space charge is trapped by the trap. Then, the electric field is removed, and the electret is successfully produced. In the second step, the instrument is shorted for 2min to remove the surface charge of the sample and stabilize the sample temperature. The temperature is raised to 250 °C (using 10 °C /min). During the heating process, the regularly arranged dipoles in the electret are de-oriented, and the trapped space charge is also detached, so the TSDC spectrum of the sample is obtained (**Figure 4-1b**). The existence of the hetero-charge confirmed the Poole-Frenkel emission under high electric field.

The sodium ion migration forms the depletion region in the OA-10G glass, and the Poole-Frenkel emission originated from the electronic conduction due to the intensified electric field is the source of the failure at high electric field. The polymer coating proposed in this study helps to mitigate the strengthening of the electric field thus improves the electric reliability of the laminate.

4.3 Electric Polarization - Electric Field Loop (P-E loop)

As discussed in section 2.3.6, the PE loop is utilized to characterize the energy density and loss at high electric field for capacitor application. As shown in **Figure 4-2a**, PE loop of as-received 10 μm OA-10G glass and FPE, polyethyleneimine (PEI), aromatic polyimides (PIs) coated polymer- glass laminates of 150ºC to 300ºC at a 200MV/cm is plotted. The derived relative permittivity values from the slopes of Figure 4-2a are shown in **Figure 4-2b,** which is consistent with the previous results discussed in **Chapter 3.** The derived loss values from the loop areas of Figure 4-2b are shown in **Figure 4-2c.** The thin layer of polymer coating does not influence the energy density or energy loss during a charge-discharge cycle.

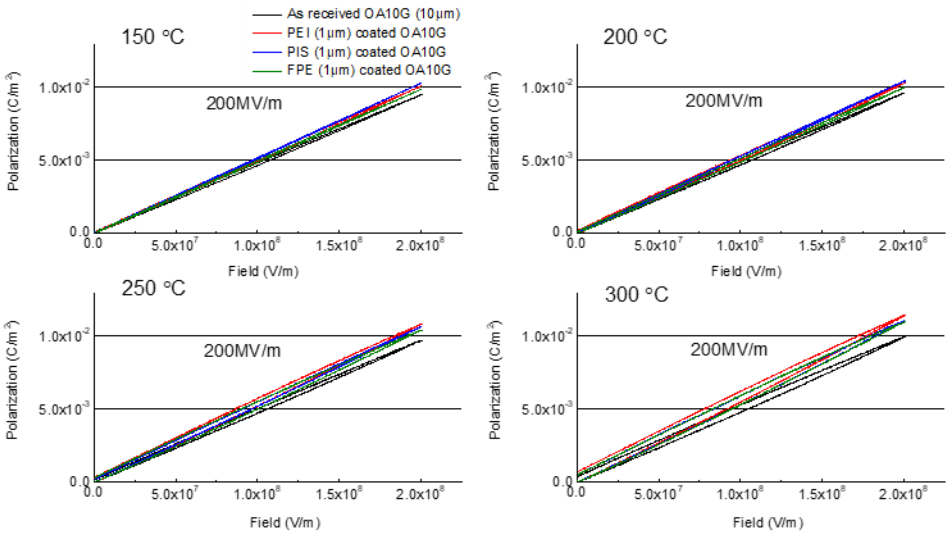

(a)

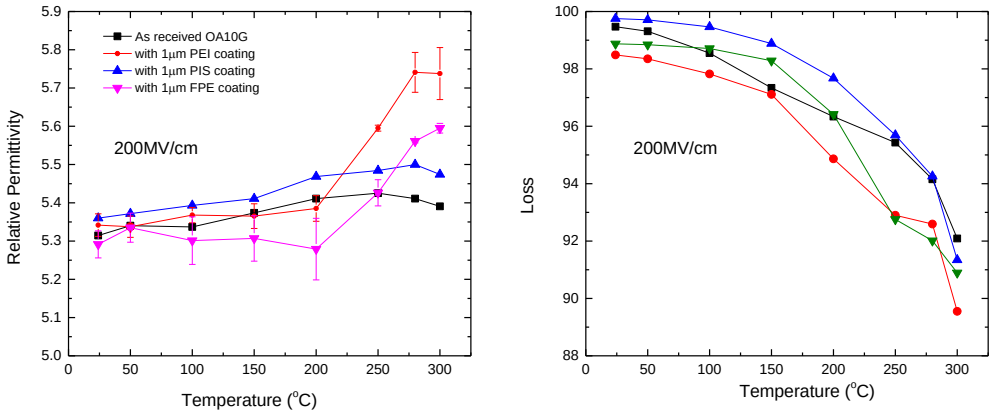

(b) (c)

Figure 4-2: (a) P-E loop of 10 μm OA-10G glass and PEI, PIS and FPE coated glass. (b) Relative permittivity of the glass and laminates. (c) Loss of the glass and laminates.

4.4 Dielectric Breakdown

High-field breakdown measurement was performed on the samples in a bath containing dielectric fluid (Galden HT-200, Solvay Solexis, Houston, TX), with 30 kV-max DC high voltage supply (Model 30/20, Trek, Lockport, NY). The voltage was ramped at a constant linear rate of 500

V/s (instrument is shown in **Figure 4-3c)**. Samples subjected to the high field measurements were coated with 50 nm Au by sputtering, with a top electrode of 2 mm diameter and a bottom electrode of 3 mm (**Figure 4-3ab**).

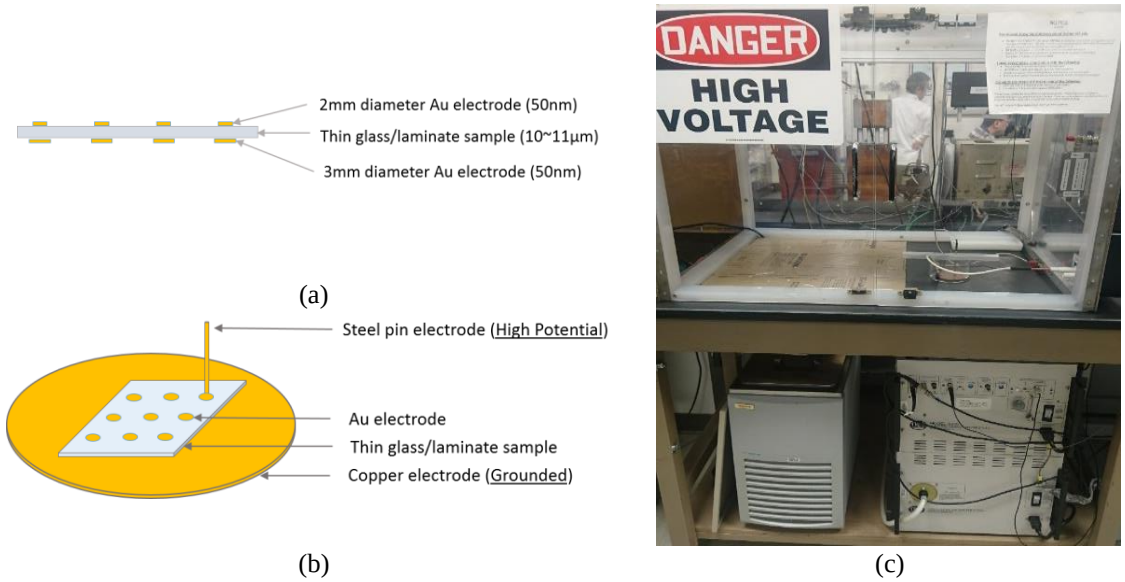

Figure 4-3: Breakdown test setup. (a) schematic of cross section view of the test sample; (b) schematic of the sample fixture; (c) breakdown test instrument.

Figure 4-4 shows the Weibull plot of the breakdown result. The most striking feature is that the slope of the Weibull plot for the polymer coated laminate is significantly increased (substantially larger β value), at both room temperature and high temperatures. As discussed in **section 2.3.5**, the Weibull modulus or shape factor β differentiates the set of breakdown data with same characteristic breakdown strength E_{BD}. The E_{BD} refers to the breakdown strength at the cumulative failure probability of 63.2%; In each set of breakdown data there is a range from the lowest failure value to the highest, and the slope β evaluate the scatter of the data.

Despite that the characteristic breakdown strength E_{BD} is not improved with the coating (cf. 10.5 MV/cm *vs.* 11.1 MV/cm at 25 °C, or 9.9 MV/cm *vs.* 11.3 MV/cm at 200 °C), the lowest measured failure electric fields for the laminate at 25 °C and 200 °C are nearly 10 MV/cm, which is equivalent to the characteristic E_{BD} of the pristine glass at 25 °C, and even larger than that at 100

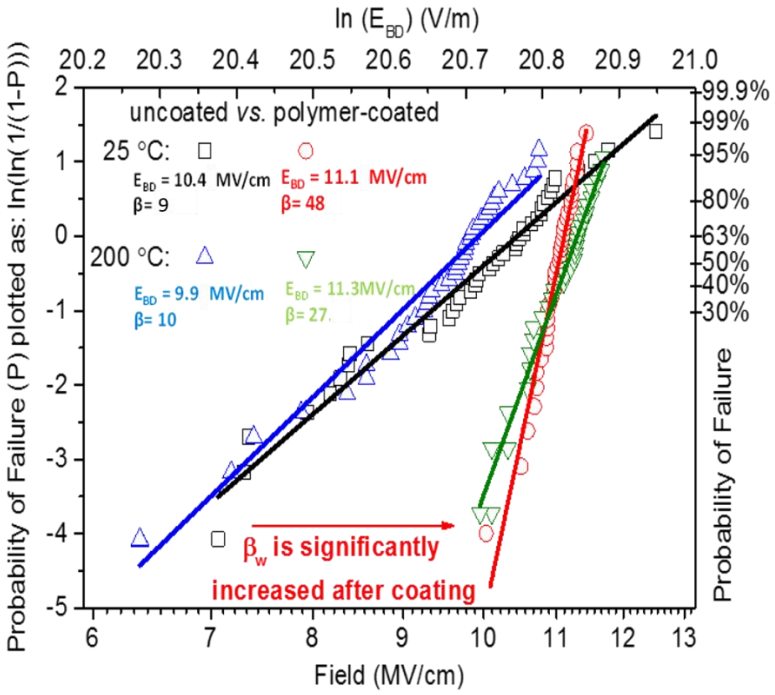

Figure 4-4: Weibull plots for the breakdown strength of as received glass and FPE coated glass at room temperature and 200°C. 50nm thick Au electrode with top area 3.1 mm^2 and bottom area 7.1 mm^2.

°C. The substantial improvement in the low probability portion of the Weibull distribution is important for the development of large power capacitors. Large β values also suggest a more uniform dielectric structure, which could effectively increase the characteristic breakdown strength E_{BD} with increasing electrode areas.

$$\frac{E_{BD-1}}{E_{BD-2}} = \left(\frac{A_2}{A_1}\right)^{1/\beta} \quad \textbf{4-1}$$

where capacitor 1 is the power capacitor and capacitor 2 is the research capacitor, A is the electrode area. **Equation 4-1** gives the empirical way to predict the reliability of large capacitors. Since E_{BD} of the polymer is negligible (0.4 MV/cm), the improved high-field properties suggest a synergistic effect in the laminate. **Figure 4-5** shows the how the scaling factor β influence the application of the glass from lab scale (3 mm diameter spot electrode) to industry scale (~100 m^2 metalized film for wrapped film capacitor). The ambient temperature breakdown strength at industry scale (100

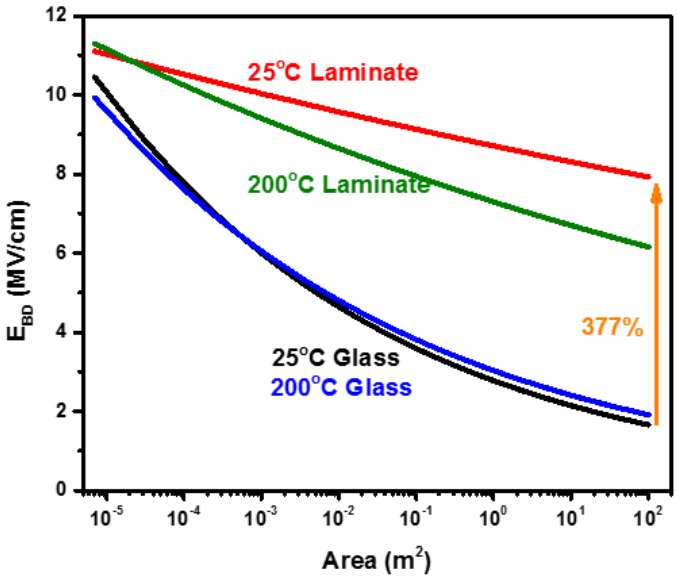

Figure 4-5: Breakdown strength from lab scale to industry. Power capacitors are in the 10 µF range and the test capacitors are in the pF range. Curves are determined from Equation 4-1.

m^2) only dropped ~30% for laminate, while the number for uncoated glass is 85%, and this significant improvement is critical in industry application. In order to further explore the effect of local electric field uniformity on dielectric breakdown mechanism of the low-alkali glass, silica nanoparticles are deposited on the glass surface. There will be increase in the local electric field inhomogeneity near the surface. 20 nm sized silica nanoparticles are sprayed over one side of the pristine glass (**Figure 4-6a**), and the electrical failures of the silica-coated glass are measured. The measurement is conducted with the silica coating facing either the anode electrode or the cathode electrode. The measured breakdown fields are plotted within the framework of Weibull statistics, as shown in **Figure 4-6b**. A schematic of the test specimen cross-section is shown in **Figure 4-6c**. Thermal poling of the low-alkali glass [2, 3] shows that with the applied electric field, sodium ions are driven towards the cathode, leaving behind a depletion layer with low conductivity thus supports most of the electric field. The thickness of the depletion layer is ~5 µm for thin low-alkali

glasses [3, 4], and the internal electric field in the depletion region is ~10 MV/cm for room temperature (extrapolation from high temperature value of 2.2 MV/cm, calculated from second-harmonic generation results) [2].

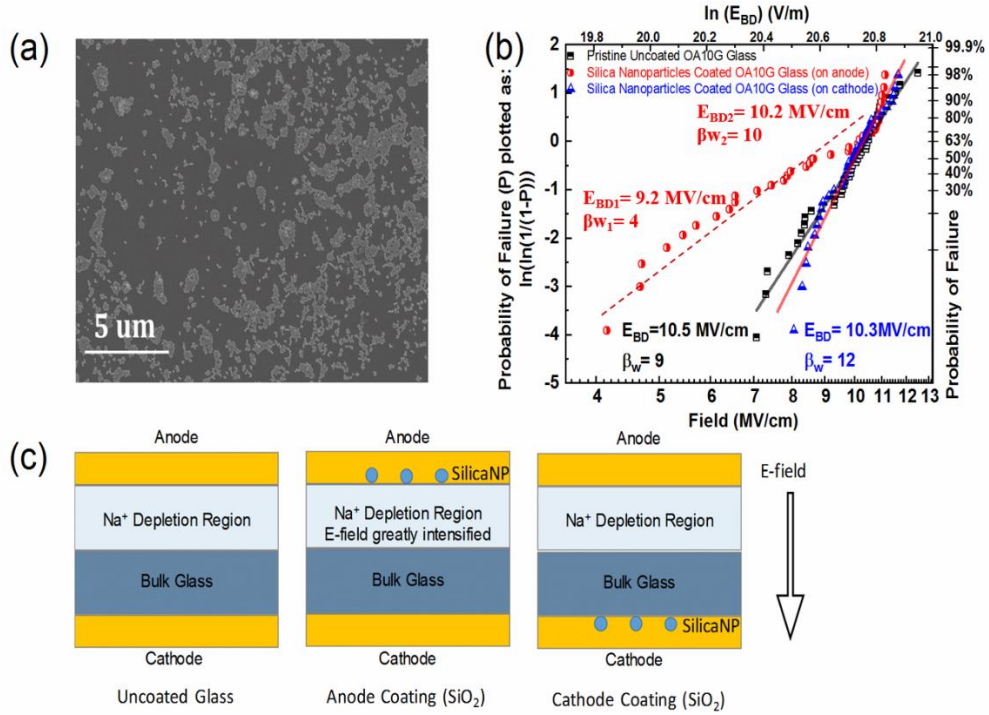

Figure 4-6: (a) SEM image of the silica coating on the glass surface; (b) dielectric breakdown strength of the pristine glass, the anode silica-coated glass, and the cathode silica-coated glass, plotted by Weibull statistics; (c) schematic depiction of the high field depletion and bulk glass regions.

The breakdown behavior of the silica-coated glass is mainly dependent on the position of the silica with respect to the field polarity. When the silica coating is on the cathode side, the Weibull plot of the coated glass is similar to that of the pristine glass. They can be well described by the unimodal Weibull distribution—the characteristic breakdown strength (E_{BD}) is measured to be 10.5 MV/cm and 10.3 MV/cm for the pristine glass and the coated glass, respectively; and the Weibull shape parameter is measured to be 9 and 12. However, when the silica coating is on the anode side, the performance is considerably deteriorated by the silica deposition, especially for the lower field failures (β_{W1}= 4) . The breakdown strengths at low probabilities of failure are dramatically reduced for the coated glass with silica on the anode side, compared to the pristine

glass and the cathode silica-coated glass. Besides, the distribution of the breakdown fields cannot be fitted with a unimodal Weibull equation, indicating the existence of an additional extrinsically controlled breakdown mechanisms.

The dependence of breakdown performance on the electrode polarity suggests that the extrinsic surface defects at the anode play an important role. On the other hand, it has been extensively studied and shown that there exists a depletion layer with substantially increased local electric fields in such glass [2, 5, 6]. The depletion layer is near the anode side, originating from the diffusion of sodium ions towards the cathode region under an applied field. The absence of sodium ions in the depletion regions accounts for the local field intensification in these regions due to a large difference in conductivities between the depletion region and bulk glass. In our previous study [7], simulation results have shown that the deposition of impurities, such as silica, on the surface of glasses, can greatly increase the local electric field beneath those impurities, e.g., up to 6 times (from 20 MV/cm to 130 MV/cm) increase in the electric field can be achieved when the particle size is on the order of 10 nm radius and of sphere shape.

As shown in **Figure 4-6c**, it can thus be envisaged that when the silica is coated on the anode side of the glass, the electric field in the depletion layer is further strengthened by the silica deposition, thus greatly increasing the chance of initiating localized electrical breakdown in this region; however, when the silica is coated on the cathode surface, the presence of a large population of mobile sodium ions can offset the electric field amplification to some extent, which could mitigate the adverse effects of the impurity introduction. In fact, both the pristine glass and the cathode silica-coated glass exhibit a similar breakdown performance, implying the electrical failures in these two glasses are very likely to be dictated by the localized breakdown occurring in the depletion layer, as the cathode coating of silica nanoparticles should not exert considerable impacts on the electric field distribution in this region. It is also worth mentioning that the multiple

breakdown mechanisms in the anode silica-coated glass could arise from the non-uniform silica coating on the glass surface. The failures at higher fields and lower fields may correspond to the regions with few and many silica particles, separately.

As a result, the double-layer-coated glass is prepared with a ~400 nm polymer layer superimposed on the silica coating (**Figure 4-7a**). **Figure 4-7b** presents the Weibull distribution of breakdown fields for the pristine glass and the coated glass. Again, the coated glass is measured twice with the coating side facing either the anode side or the cathode side.

As expected, the polymer coated glass with silica particles on the cathode side behaves similarly to the pristine glass with E_{BD} of 10-11 MV/cm and β_w ranging from 9 to 12. When the polymer coating is on the anode side, overlaying the silica nanoparticles, the improved dielectric breakdown strength is attributed to the reduction of the electric field in the depleted region (**Figure 4-7c**). Moreover, it is interesting to note the breakdown performance of the anode double-layer coated glass even exceeds that of the pristine glass, i.e., E_{BD} and β_w of the double-layer coated glass is 11.2 MV/cm and 58, respectively; while they are measured to be 10.5 MV/cm and 9 for the pristine glass. The polymer coating not only mitigates the adverse impacts imposed by the silica nanoparticles but also reduces the influences of other extrinsic defects (i.e. dust particles) preexisting on the surface of the pristine uncoated glass.

The pristine glass is also coated with polymer and its breakdown strength is compared with that of the uncoated glass, as shown in **Figure 4-8**. E_{BD} can be slightly improved by the polymer coating, increasing from 10.5 MV/cm for the uncoated glass to 11.1 MV/cm for the coated glass;

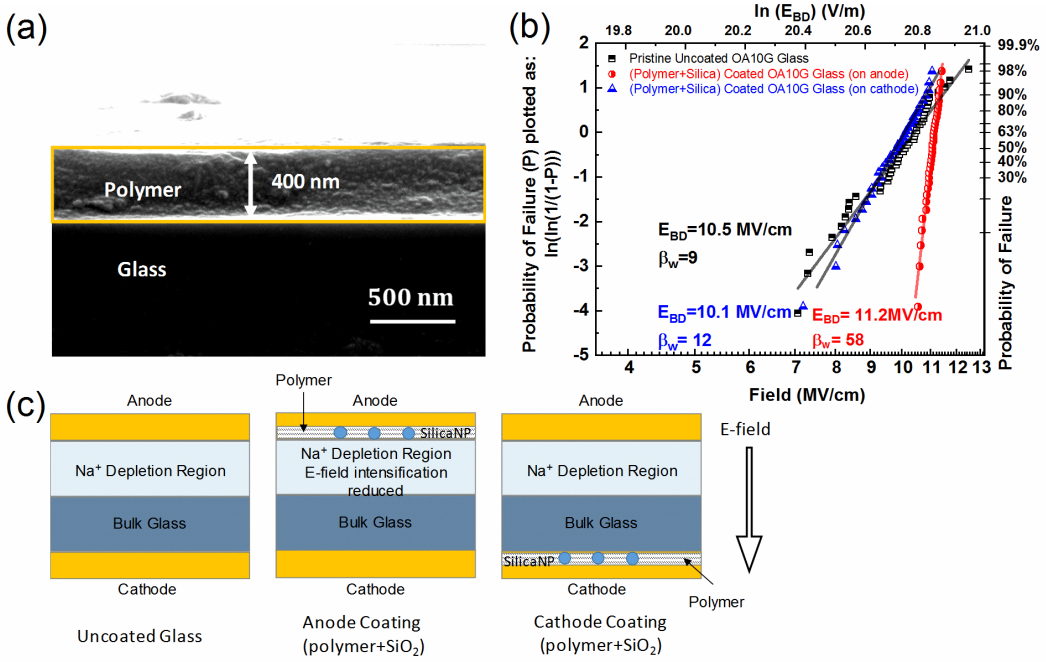

Figure 4-7: (a) SEM image of the polymer coating on the glass; (b) dielectric breakdown strength of the pristine glass, the anode polymer/silica-coated glass, and the cathode polymer/silica-coated glass, plotted by Weibull statistics; (c) schematic depiction of the electric field distribution in the depletion layer.

but what is more impressive is the significantly enhanced β_w: the β_w shape parameter for the pristine glass is 9 and increases to 49 for the polymer-coated glass laminate. The large β_w indicates a dramatic improvement in the low field failure, which has important implications for the reliability of dielectric materials. For instance, the breakdown field corresponding to 10% probability of failure is degraded to 8.0 MV/cm for the uncoated glass, but it is still maintained at 10.7 MV/cm for the coated glass, which is even greater than the characteristic breakdown strength of the uncoated glass. Moreover, the silica/polymer double-layer coated glass demonstrates a similar high field behavior to the polymer-coated glass, suggesting the polymer coating can tolerate the presence of various impurities (e.g., silica particles and preexisting dust particles on the glass surface) and reduce their adverse effects to the same level. This observation also implies improved reliability in the application of these dielectric glasses, as different types of impurities or defects

introduced during the production and assembly of these materials can be alleviated by a final polymer coating.

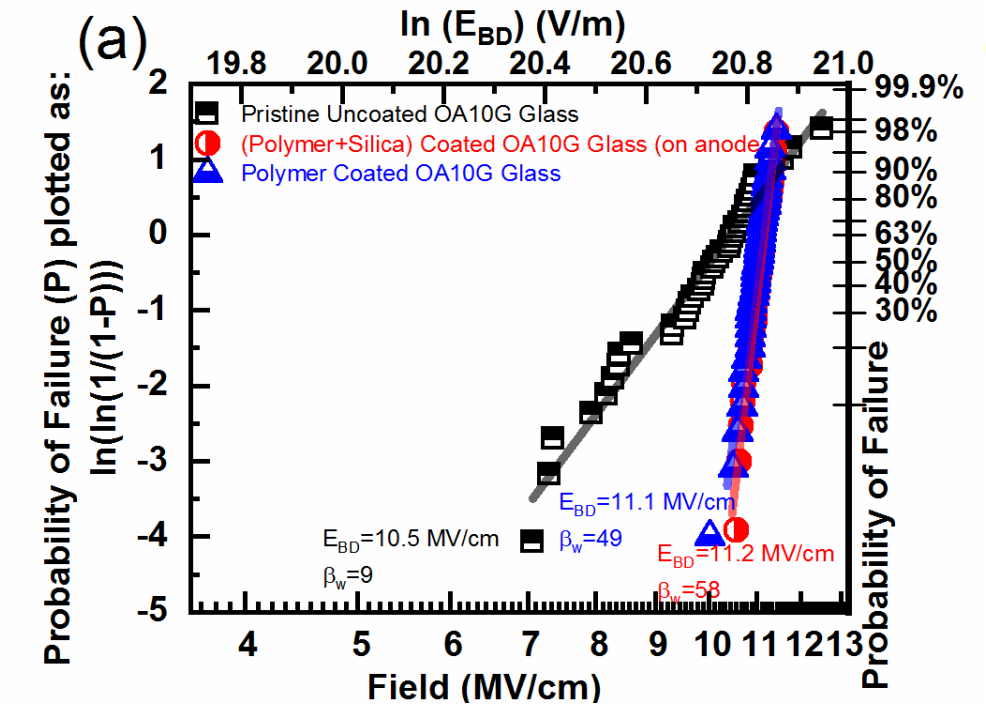

Figure 4-8: Dielectric breakdown strength of the pristine glass, the polymer/silica-coated glass, and the polymer-coated glass plotted by Weibull statistics.

4.5 Breakdown After Thermal Poling

As shown in **Figure 4-9a**, the slope of the Weibull plot for the coated-laminate is significantly increased (substantially large β value). Despite the nominal breakdown strength (E_{BD}) is not improved much with the coating (cf. 10.5 MV/cm *vs.* 11.1 MV/cm), the lowest measured failure e-fields for the laminate are nearly 10 MV/cm, which is equivalent to the characteristic E_{BD} of the pristine glass, thus it has great implication for the industry application. Due to the nature of the fast

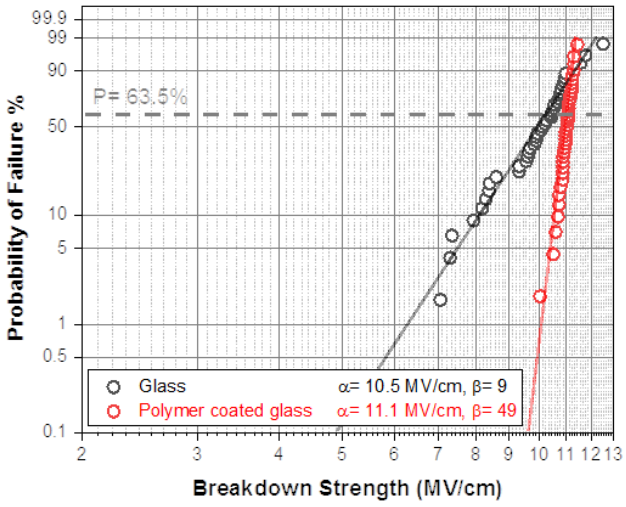

(a)

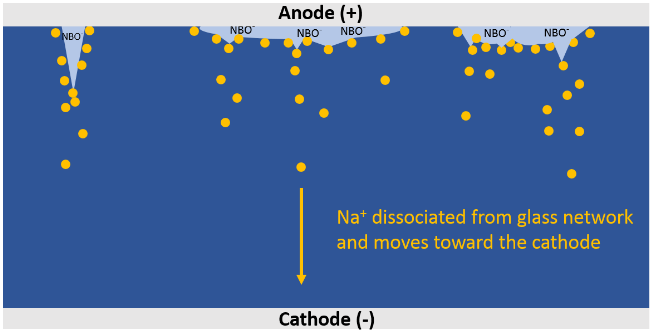

(b)

Figure 4-9: (a) Weibull Statistic of the breakdown of glass and polymer coated glass; (b) Schematic drawing of the sodium depleted layer during breakdown.

ramping rate of breakdown test (500V/s), it is hypothesized that the sodium depletion region is nonuniform over the anode area. The depleted sodium ions are driven towards the cathode, leaving behind a partially depleted uniform non-bridging oxygens networks with much lower conductivity and thus act as "defects" in the glass under high electric field (**Figure 4-9b**).

After the long-time thermal poling (0.5 MV/cm, 250 ºC, 1- and 5-days using HALT system), the glass and laminate breakdown results are shown in **Figure 4-10a**. The characteristic

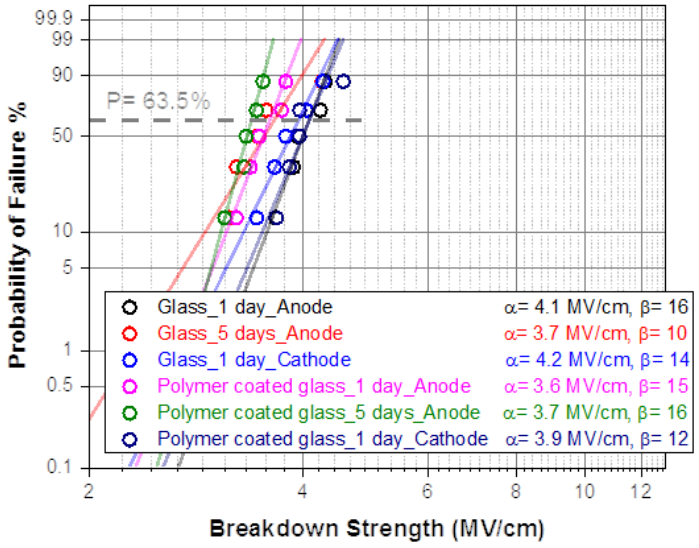

(a)

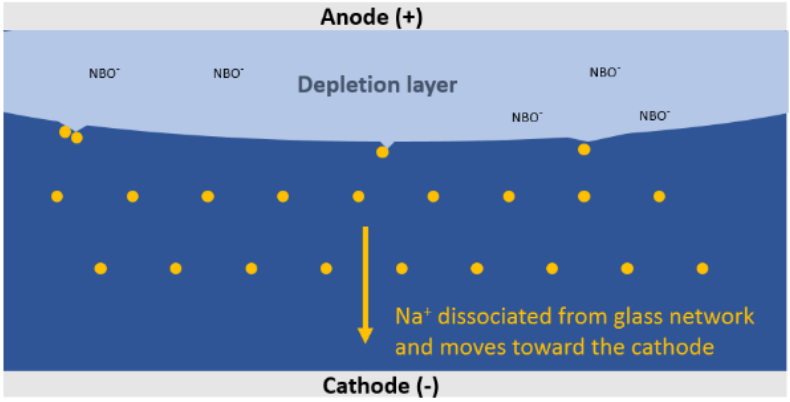

(b)

Figure 4-10: (a)Weibull Statistics of long time poled (using HALT system) 20μm glass and polymer coated glass samples. The poling temperature and voltage is 250ºC and 1000V independently; (b) Schematic drawing of the sodium depleted layer during long time poling.

breakdown field (α) and Weibull modulus (β) of both pristine glass and polymer coated glass are basically the same and are highly reduced from non-poled sample (~10MV/cm), and the poling polarity (anode side and cathode side) has no effect on the breakdown strength or Weibull modulus, implying the breakdown is induced from a bulk effect, not charge injection. The impedance spectroscopy results suggest a uniform depletion layer after long time poling. When the low-alkali glass is exposed to a longer time (compared to breakdown) thermal poling, with the applied electric field, sodium ions are driven towards to cathode, leaving behind the glass network with a uniform depletion layer (**Figure 4-10b**) with a lower conductivity thus supports most of the electric field and the breakdown is dominated by sodium depletion layer.

4.6 Different Polymer Coating

In addition to the FPE coating, high T_g polymer-cellulose has been coated using the same dip coating method to verify the improvement of polymer coating. **Figure 4-11** shows that the Weibull modulus increase (7 for uncoated glass) significantly after a thin layer of cellulose coating at room temperature and 200ºC (β= 44 at room temperature and β= 56 at 200 ºC). This is in consistent with the conclusion given in the previous section that it is the layer of a polymer, independent of the what kind of polymer it is, that help improve the reliability of the glass dielectrics.

4.7 Conclusions

The electrical failures of the low-alkali boroaluminosilicate glass is affected by the depletion layer. The sodium ion migration forms the depletion layer in the OA-10G glass, and the Poole-Frenkel emission originated from the electronic conduction due to the intensified electric field is the source of the failure at high electric field. The polymer coating on the anode side of the

glass proposed in this study helps to mitigate the strengthening of the electric field in the depletion layer.

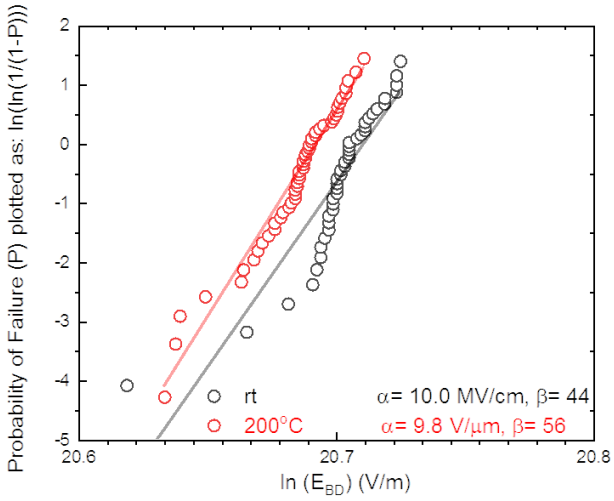

Figure 4-11: Weibull Statistics of 3wt.% cellulose coated 20 μm OA-10G glass samples tested at rt and 200 °C.

The high electric field properties, especially the electrical reliability, are improved, which is manifested by the significantly increased breakdown strengths at low probabilities of failure and by the great tolerance of defects and its effect is independent of the polymer. This may due to the local electric field intensification around the "defect" region, and this will be further confirmed by simulation of the electric field distribution in the following chapter. It should be noted that the error of polymer coating thickness mentioned in **section 2.2** would introduce error in breakdown results as well.

4.8 References

1. Dash, P., et al., High electric field conduction in low-alkali boroaluminosilicate glass. *Journal of Applied Physics*, 2018. **123**(5): p. 054102.

2. Smith, N.J., M.T. Lanagan, and C.G. Pantano, Thermal poling of alkaline earth boroaluminosilicate glasses with intrinsically high dielectric breakdown strength. *Journal of Applied Physics*, 2012. **111**(8): p. 083519.

3. Dash, P., Dynamics of Space Charge Polarization and Electrical Conduction in Low Alkali Boroaluminosilicate Glasses. 2013.

4. Murata, T., et al., Electrode‐Limited Dielectric Breakdown of Alkali Free Glass. *Journal of the American Ceramic Society*, 2012. **95**(6): p. 1915-1919.

5. Dash, P., et al., Activation energy for alkaline-earth ion transport in low alkali aluminoborosilicate glasses. *Applied Physics Letters*, 2013. **102**(8).

6. Choi, D.H., Numerical modeling of space charge dynamics and electrical breakdown in solid dielectrics. 2013, The Pennsylvania State University.

7. Yuan, M., et al., Electrical Reliability of Polymer Enhanced Glass Dielectrics. US-Japan Conference Proceedings, 2017.

Chapter 5
Electric Field Distribution Simulation

5.1 Introduction

In the previous chapters the high electric field and low electric field properties of the low-alkali boroaluminosilicate glass and polymer-glass laminate has been explored. In this chapter, the local electric field distribution around the glass depletion region is simulated and to understand the role of nonuniform sodium migration on local field enhancement. The finite element method (FEA) using the ANSYS® Electromagnetic software is briefly introduced in **section 5.2**. The overall electric field distribution is presented in **section 5.3**, followed by the simulation of two different models – particle/defect (**section 5.4**) and streamer (**section 5.5**) and the comparison with previous experimental work in **Chapter 4**.

5.2 Finite Element Analysis (FEA) and Ansys Software

The basic process of the finite element analysis method is to discretize the continuous medium into a group of units, transforming the infinite degree of freedom problem into a finite degree of freedom problem, and then solving it by computer. The basic process of the finite element analysis method is:

(1) Discretization of continuous fields. In order to use the finite element method to analyze the electric field, the continuous field is first discrete, that is, the continuous field is divided into a finite number of unit bodies. For a planar field unit, it may be a triangle, a quadrangle, etc. The shape of the space problem unit may be a tetrahedron, a rectangular parallelepiped or a hexahedron. The vertices of each small unit and other representative points in the small unit become the nodes

of the unit. The smaller the finite element is divided, the smaller the deviation between the calculated result and the actual value. However, the amount of calculation will be greatly increased, which leads to longer calculation time.

(2) Establish a field variable model of the small unit. According to the characteristics of the field variables to be obtained, a model of the field variables to be obtained is established to describe the change of the field variables to be obtained in each small unit. The field variable model established here only approximates the true field variable distribution. When building a field variable model, interpolation polynomials for field variables at nodes are often used, since polynomials are easy to integrate and differentiate.

(3) Determine the unit characteristics. Once the unit model has been established, that is, the unit shape and its field variable model have been selected, a matrix formula representing the characteristics of each unit can be determined.

(4) Collect unit characteristics and obtain equations according to the defined solution conditions. In order to determine the characteristics of a system-wide model consisting of a unit network, all unit characteristics must be "collected". In other words, we must group expressions that represent cell properties to form a matrix equation that represents the properties of the entire solution domain. In general, the assembly process is based on the principle that at some nodes where the units are connected to each other, since the nodes are common to these units, it is required that all the adjacent units at the node have the same field variable at the node. Then, according to the definite condition, the matrix equation about the whole solution domain property obtained from the collection of all unit characteristics can be transformed into a system of equations about the value of the node field variable.

(5) Solve the equations. After the simultaneous equations of the full solution domain are obtained, the equations can be solved to obtain the field variable values of the unknown nodes.

Through these node values, the value of any point field variable in the field can be obtained from the field variable model of each small unit [1-3].

FEA is a computerized method that can be used to predict how a product would react to loads (electrical, mechanical, thermal, etc.). By subdividing a large problem into smaller and simpler parts (finite elements) through meshing, it avoids a large amount of numerical calculation. Thus, it's a general way to solve the partial differential equations of the Maxwell equations. In this study, we will use ANSYS software to conduct the electric field simulation.

ANSYS® is a professional software development company mainly engaged in the development of various engineering application software. Its software products can simulate engineering structures, electromagnetic, thermal, fluid, coupled fields or multiple physics. It can also analyze simulation results, optimize physical parameters according to the technical requirements of users. The user only needs to establish the geometric model and assign the boundary conditions. ANSYS's electronics analysis software can calculate the static electromagnetic field and dynamic electromagnetic field distribution of the designed device or device, magnetic flux density, magnetic field density, magnetic moment and current density, charge density, electric field distribution and other physical parameters. **Figure 5-1** shows the procedure of solving a project [4, 5].

5.3 Electric Field Distribution of Bulk Sample

The electrical conductivity ratio between the depletion region of the glass and bulk glass in this study is assumed to be 1/8.7 (see Chapter 3.3 for detailed calculation). The conductivity of the bulk glass: $1e^{-11}$S/m. The conductivity of the polymer is calculated based on the electric flux density at the glass/polymer interface: $5.7e^{-12}$S/m. **Figure 5-2** shows the electric field distribution

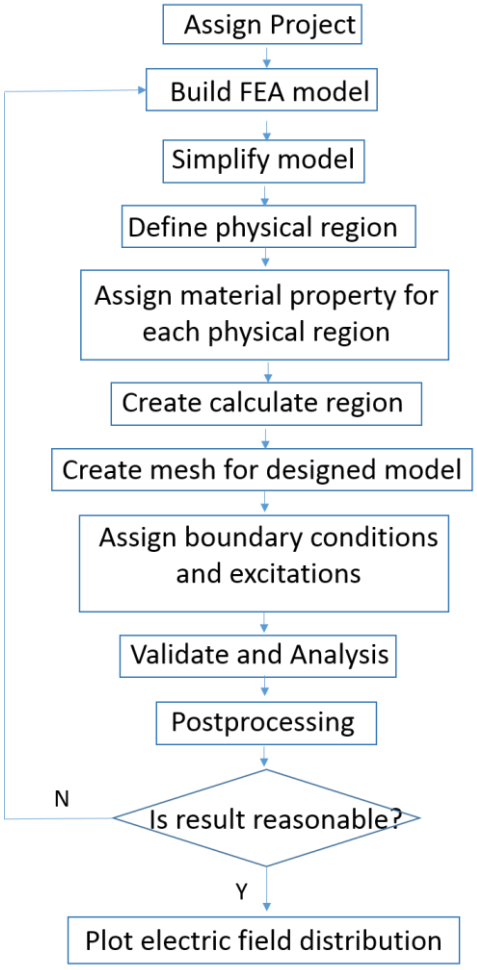

Figure 5-1: Procedure of finite element analysis on electric field distribution of glass/laminate [4].

at different layer (depletion layer, bulk glass and polymer layer). The magnitudes of the electric fields are based on conductivity differences.

5.4 Local Electric Field Distribution of Particle/Defect Sample

Figure 5-3 shows the model of the electric field distribution simulation of a defect sample using Ansys Maxwell® software.

Figure 5-3ab shows the simulation models for glass and laminate, and only the geometry in the vicinity of the cone shape glass defect (r = h = 5nm) is modeled. The 1/2-cylinder shape geometry is analyzed due to the symmetry and display convenience. The finite element meshes **Figure 5-3cd** is automatically generated using ANSYS Maxwell® preprocessor software and the carefully refined in the vicinity of the cone shape defect. Mesh size density has been evaluated to ensure the simulation accuracy.

The excitation voltage is applied on the top electrodes and the bottom electrodes are zero potential. Electric field simulation is based on the electrical conductivity of the materials. The applied voltage for the bulk samples is assumed to be 11kV, which is close to the E_{BD} in the breakdown experiment. At such high electric field, the sodium content of the glass at the vicinity of the anode would migrate towards the cathode thus form a cation depletion layer with a magnitude higher electric field compared to the bulk of the glass [5]. The voltages applied on the simulated geometry are 40V and 83.6V for glass and laminate.

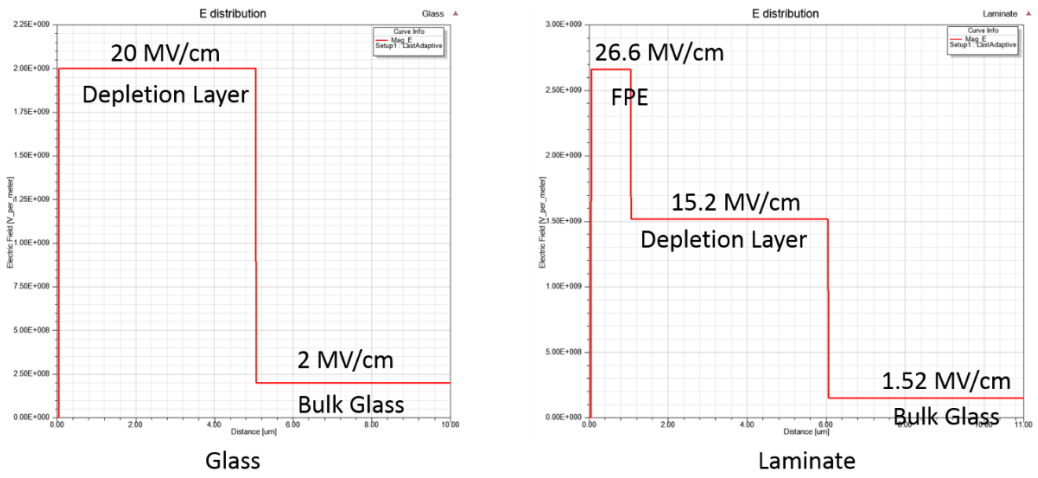

Figure 5-2: Electric field distribution of depletion layer and bulk glass for (a) 10 μm glass and (b)11 μm laminate under 11kV voltage.

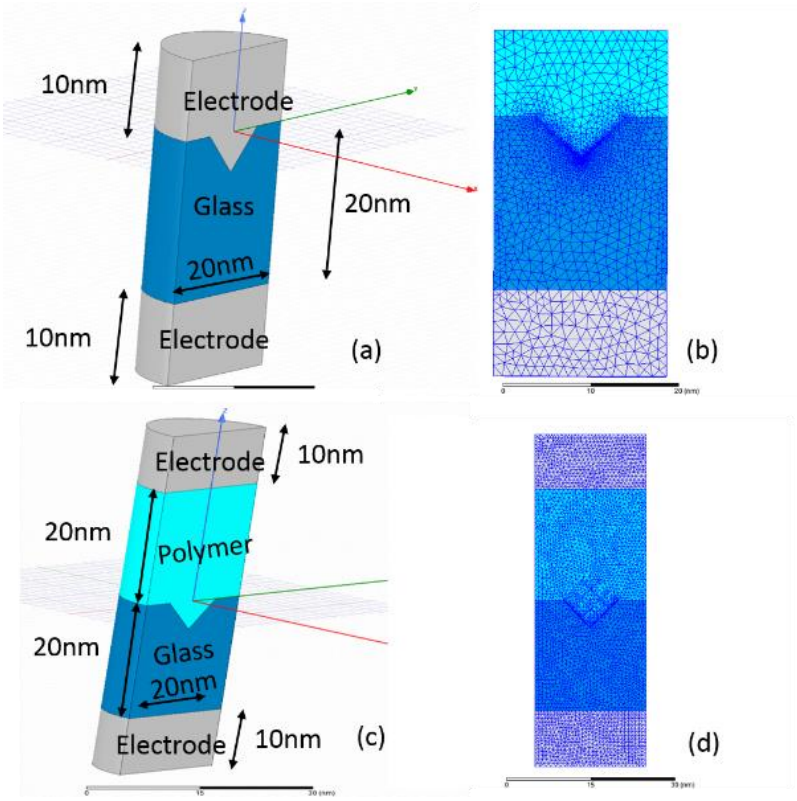

Figure 5-3: Modeled geometry and cross-section view of the complete 3D mesh: (a)(b): Glass; (c) (d) Laminate.

As shown in **Figure 5-4a**, the maximum electric field is distributed around the defect tip for the uncoated glass but shifted to the circumference of the base of the defect (the perimeter of the cone base) for the coated laminate. The simulation results can be qualitatively understood by analogy with a point discharge process (also known as corona discharge). In the uncoated glass, the defect filled with electrode metals would serve as a pointed conductor (the electrode metal has higher conductivity than the glass); the local electric field around the defect tip (the place with the highest curvature) could be significantly enhanced. As expected, discharge or electrical treeing is more easily to initiate from this point. In the coated glass, the existence of the polymer turns the underneath glass to be the equivalent pointed conductor (due to lower permittivity of the polymer than that of the glass). The points with the largest curvature are thus shifted from the cone apex to the base perimeter, along which the maximum electric field is distributed. Additionally, the

maximum field in the pristine glass is more than one order of magnitude larger than that of the laminate (**Figure 5-4b**), which is at least partially associated with the reduced curvature of the protrusion (points) for the coated glass.

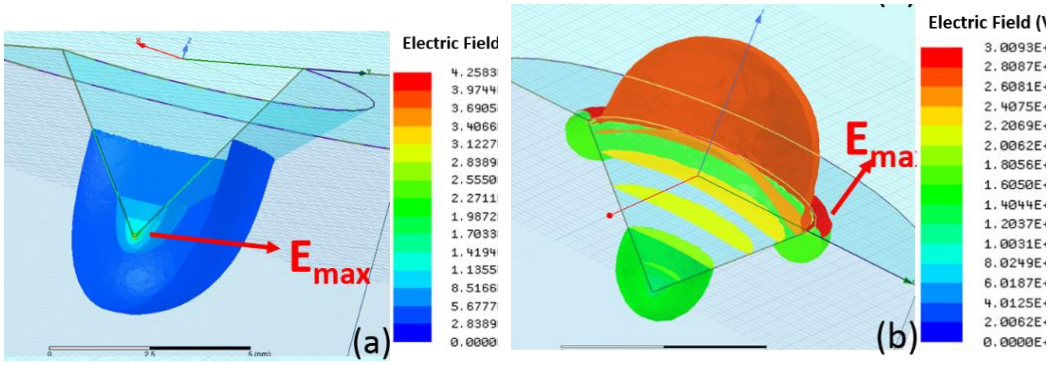

(a) (b)

Figure 5-4: Electric Field Distribution in the vicinity of the cone shape defect: (a) Glass model; (b) Laminate model.

As for the particle model, since the dielectric breakdown for the anode silica-coated glass is attributed to the electric field intensification in the depletion layer, approaches to reduce the enhanced E-field should improve the breakdown performance of the silica-coated glass. The vicinity (50 nm of the depletion region/polymer layer) of the particle defect (of 10 nm radius and of sphere shape) area has been modeled. The excitation voltage is applied on the top electrodes and the bottom electrode are zero potential. The applied voltage for the bulk samples is assumed to be 11 kV. The simulation results in **Figure 5-5a** have shown that the deposition of impurities on the surface of glasses, can greatly increase the local electric field beneath those impurities, showing as red lines, while after a thin layer of polymer coating, the maximum local electric field is around the particle showing as green lines in **Figure 5-5b** and has been reduced to about 1/2 of the uncoated The actual values of the local field are probably overestimated in the simulation due to local conduction in the high field regions.

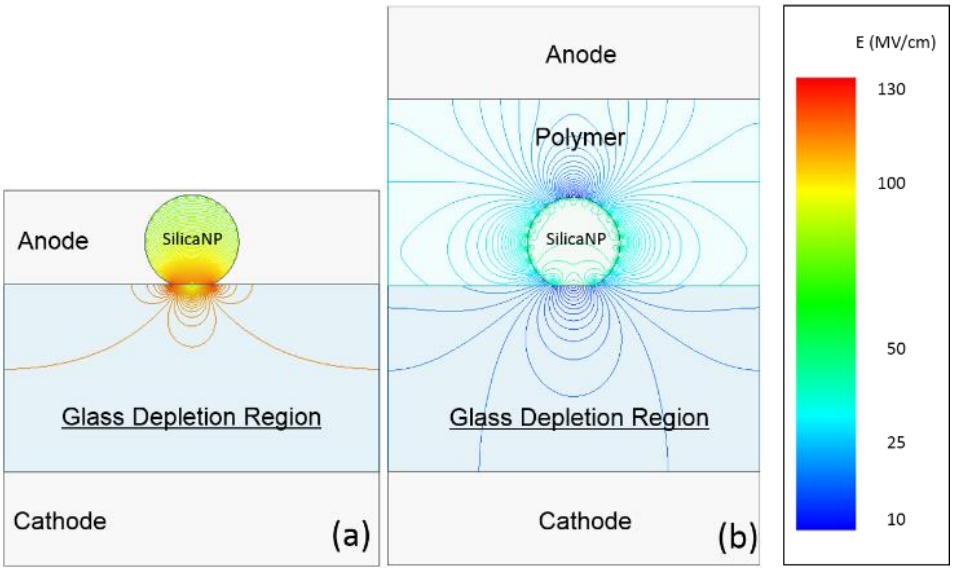

Figure 5-5: Ansys Maxwell simulation of the electric field distribution of (a) silica-deposited glass and (b) polymer/silica double layer coated glass.

5.5 Local Electric Field Distribution of Streamer Model

As per discussed in **Chapter 4**, the simulation of the electric field distribution in Figure **5-6** shows that the maximum local electric field around these "defects" are greatly reduced (from 103 MV/cm to 39 MV/cm) after the polymer coating for an applied electric field of 10MV/cm, thus the chance of initiating a breakdown event is reduced. The simulated local values of electric field are higher than the applied breakdown values (100 MV/cm for local versus 10 MV/cm for applied). Local field breakdown of glass has been studied though pulsed laser techniques and values of 30 MV/cm have been measured. Depending on the adjacent material next to the glass (metal versus polymer) there is significant difference in the magnitude of the local electric field.

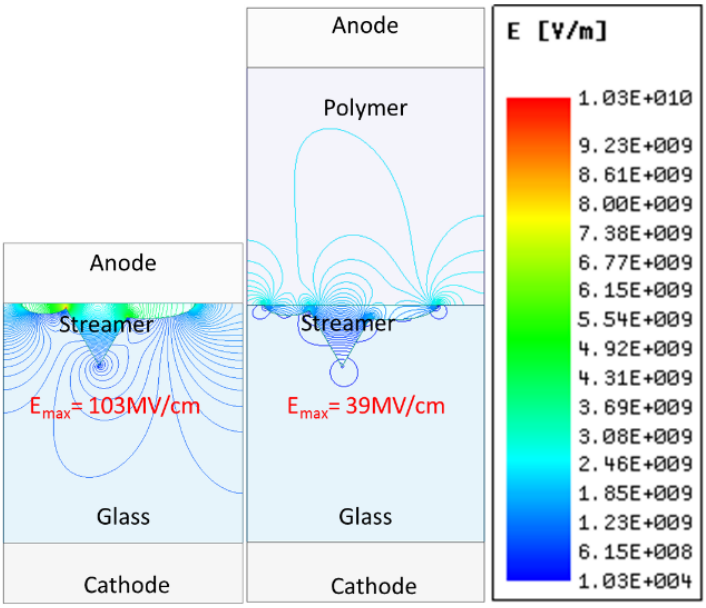

Figure 5-6: Simulation results on the electric field distribution around the sodium depleted region for glass and polymer-glass "defect".

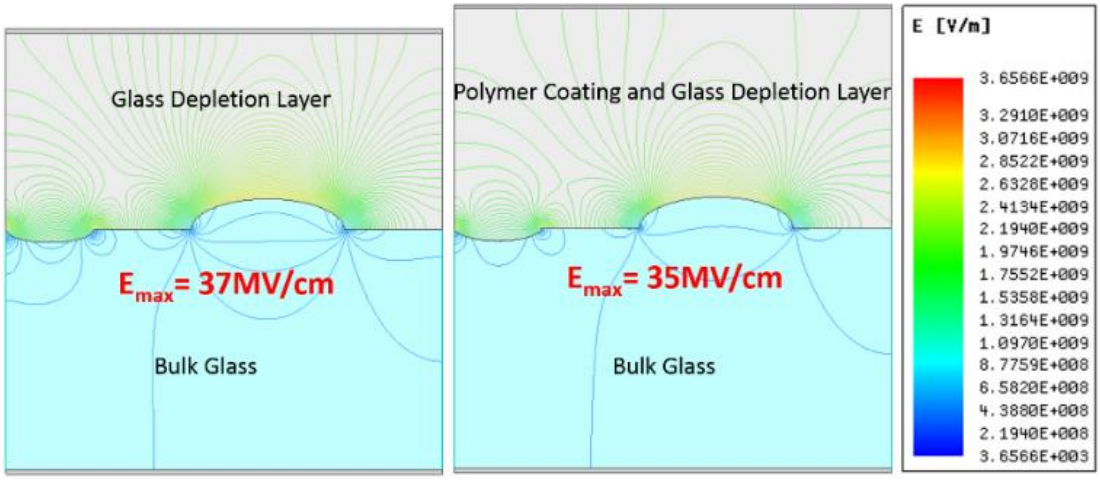

Figure 5-7: Simulation result on the electric field distribution around the sodium depleted region for glass and polymer-glass laminate.

The simulation of the electric field distribution after HALT poling in **Figure 5-7** shows that the maximum local electric field does not change after the polymer coating, implying that the polymer layer is not effective in modifying electric field distribution for degraded samples.

5.6 Conclusions

The electrical failures of the low-alkali boroaluminosilicate glass are primarily affected by the greatly intensified electric field in the depletion layer. Application of a polymer coating on the anode side of the glass can reduce the electric field intensity in the depletion region. The high field properties, especially the electrical reliability, are improved, which is manifested by the significantly increased breakdown strengths at low probabilities of failure and by the great tolerance of defects.

5.7 REFERENCES

1. Hughes, T.J., The finite element method: linear static and dynamic finite element analysis. 2012: Courier Corporation.

2. Cook, R.D., Concepts and applications of finite element analysis. 2007: John Wiley & Sons.

3. De Borst, R., et al., Nonlinear finite element analysis of solids and structures. 2012: John Wiley & Sons.

4. Barbero, E.J., Finite element analysis of composite materials using ANSYS. 2013: CRC press.

5. Madenci, E. and I. Guven, The finite element method and applications in engineering using ANSYS®. 2015: Springer.

Chapter 6

Conclusions and Future Work

6.1 Conclusions

In **Chapter 1** of this dissertation, a brief introduction of common capacitor materials and their essential criteria has been presented and a new potential capacitor material – low-alkali boroaluminosilicate glass – has been brought up to compare with the commercialized ones. The fundamentals of the dielectric materials have also been introduced here to give a background on the proposed dielectric laminate material in this study. The energy density equation $U_e = ½ \varepsilon_o \varepsilon_r E_{BD}^2$ relates the energy density of a dielectric material with its permittivity and characteristic breakdown strength and these two parameters will be investigated in this study. This chapter concludes with a problem statement and the organization of the dissertation.

Chapter 2 mainly describes the ways explored to achieve the desired thickness and uniformity coating and provides a in-depth understanding of the main dielectric characterization method utilized in this study to understand the conduction mechanism of the proposed laminate.

Low electric field (under 1Volt) characterization of dielectric relaxation spectroscopy (DRS) and AC impedance spectroscopy (IS) has been discussed in **Chapter 3**, the results implied that the proposed polymer coating does not affect the permittivity or dissipation factor of the state-of-art low-alkali boroaluminosilicate glass, thus would not dilute its energy density. The calculation of the sodium depleted region thickness has been introduced here to support the electric field simulation study in **Chapter 5**.

Chapter 4 investigates the conduction mechanism of glass and glass-polymer laminate under high electric field. Thermally Stimulated Depolarization Current (TSDC) measurement of

the glass support the conclusion – the conduction mechanism of the sodium depletion layer under the high electric field is Poole-Frenkel, and polymer coating help reduce the high electric field intensification in depletion layer. P-E loop verified the conclusion from **Chapter 3** that polymer coating does not change the permittivity, thus the energy density of the dielectric is not influenced. The results of dielectric breakdown and breakdown after long time thermal poling suggested that the electrical failure of the glass is affected by the sodium depleted layer – trace amount of sodium depleted from anode electrode side towards cathode electrode side under high electric field. The local electric field distortion by local defects (partials or "streamers" caused by nonuniform sodium ion movement) attributes to this conduction mechanism and this is consistent with the electric field simulation result presented in **Chapter 5**. The thin layer of polymer coating proposed in this study could significantly improve the reliability of the potential dielectric material thus further improve the energy density by mitigating the local defects.

In **Chapter 5**, the local electric field around the "defects" explored in **Chapter 4** had been simulated using ANSYS® Maxwell software, identical conclusions were obtained thus the high electric field failure is attributed to the local electric field enhancement caused by local "defects" and could be significantly reduced by a thin layer of polymer coating.

6.2 Original Contribution

Throughout the completion of this dissertation work, the following original contribution has been made to the field of high temperature energy storage dielectric materials:

1) Electrical reliability improvement by polymer coating: Previous effort has been made to study the mechanical reliability improvement of the glass material [1-3], but to the best of my knowledge, the significant Weibull modulus (β) improvement represented in **section** Error! Reference source n ot found. has not yet been reported. The increased β value indicates a more reliable dielectric

material for potential capacitor application, since the lowest breakdown events would be significantly improved, and the laminate would have a very narrow dielectric breakdown strength range. The improved β value also has great implication on breakdown strength when scaling from lab scale to industry scale due to the scaling law.

2)Correlate the dielectric breakdown experimental work with electric field simulation result to understand the electrical failure mode in low-alkali boroaluminosilicate glass: The improvement of Weibull modulus after polymer coating discussed in **section** Error! Reference source not found. a nd **section 4.5** implied that the local electric field enhancement caused by either glass surface particle/defect or nonuniform sodium depleted region, coinciding with that obtained by simulation results in **section 5.4** and **5.5**. The simulations provided a theoretical framework for understanding how local electric field intensity around defects in glass is suppressed with a polymer coating.

6.3 Future Work

6.3.1 Mechanical Breakdown: Ring-on-Ring Test

To study the impact of surface defects on mechanical/electrical breakdown strength, a mechanical testing method that evaluates the same part of the specimen (with the metal electrode on) as the dielectric breakdown testing is proposed. Previous analyses were carried out by means of the two-point-bending test and the mechanical failure was attributed to the flaws at the cut edges of the glass ribbon. In order to eliminate the influence of edge defects a ring-on-ring test is a widely used method to determine the fracture strength of a brittle material in plate geometry (**Figure 6-1**) [4]. For this geometry, the applied stress is far away from the edges so that only the surface defects in the glass will influence the mechanical properties. Furthermore, the finite element analysis

(FEA) is adopted here to model both the glass deflection and stress distribution, thus leading to a better understanding of the converting between failure load and failure stress.

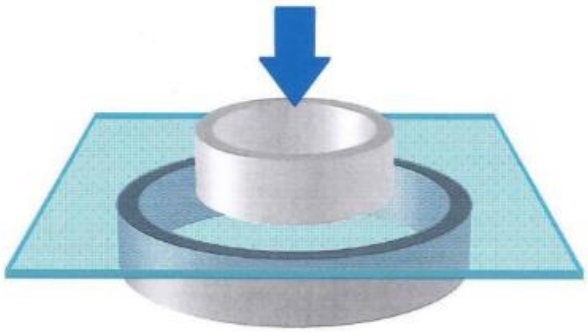

Figure 6-1: Schematic of Ring on Ring Test

Figure 6-1 schematically shows an ASTM standard ring-on-ring test: A thin glass specimen (76.2mm square plate) is sandwiched between two concentric rings, where the bottom ring (D= 30 mm) remains and serves as the support ring [4]. The top ring (D= 15 mm) is connected to a load rod and apply pressure on the specimen glass with a constant rate. Force sensor (incorporated on top of the glass within the load ring) and a deflection sensor (settled right below the center of the glass specimen) will monitor the stress and deflection until the fracture occurs. The maximum stresses calculated will be analyzed through Weibull statistics [5]. Coupled with the two-point bending tests, the edge defects can be deconvoluted from all defects [6].

The ASTM standard for the ring-on-ring test specifies that the deflection of the specimen does not exceed a quarter of its thickness before fracturing, however, this is not the case for thin specimens. When the deflection exceeds the limit (25%) the membrane stress will be induced from inside in order to compensate the load force that leads to larger deflection. In such a case, the small deflection theory (linear bending, adopted by ASTM standard to convert failure load to failure stress) that assume no membrane stress is not valid since it significantly overestimates the bending stress, and the large deflection (nonlinear) effect starts to dominate.

FEA is a computerized method that can be used to predict how a product would react to loads (mechanical, electrical, thermal, etc.). By subdividing a large problem into smaller and simpler parts (finite elements) through meshing, it avoids a large amount of numerical calculation.

Thus it's a straightforward way to solve the large deflection problem without getting into details to solve the nonlinear equilibrium equations containing membrane forces. Below is a modeling of the ring-on-ring test using Ansys® software. The elastic properties of the specimen glass used for the modeling are:

E= Young's modulus= 72.5 GPa

v= Poisson's ratio= 0.23

Load= 100 N

As shown in Figure 6-2(a), meshing creates enough finite elements to conduct the modeling. The max principle stress (Figure 6-2(b)) indicates the max tensile stress of the glass specimen under equivalent load, while the peak stress (where the fracture starts to initiate) occurs in the center of the specimen.

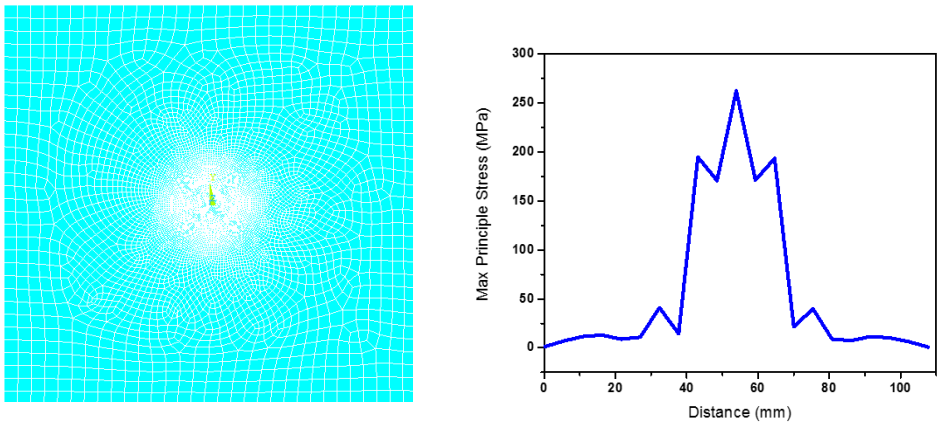

(a) (b)

Figure 6-2: Shell element FEA model mesh (a) and the max principle stress distribution along the diagonal line.

6.3.2 Highly Accelerated Life Test (HALT)

The Highly Accelerated Life Test (HALT) is a process for revealing design flaws and deficiencies by using high and low temperature transformed oscillating systems for electronic and mechanical assemblies. The purpose of HALT is to identify product functionality and damage limits in the early stages of product development to optimize product reliability.

In the product development process, a test designed to derive product design margin and ultimate load carrying capacity, which applies a stepwise method to apply environmental stress to the product and test its performance until the product fails. In order to improve the test efficiency, the applied stress is not the simulation of the working environment but the accelerated stress, usually the temperature cycle of high temperature change rate and the multi-axis random vibration, and includes electrical stress such as energization cycle, low voltage, frequency deviation etc. The electric limit values obtained by the highly accelerated life test can be used as the criteria for predict the lifetime of the capacitors.

The mean time to failure (MTTF) of a device under a voltage (V) and temperature (T) could be modeled though an empirical relationship established by Prokopowicz and Vaskas [7]:

$$\frac{t_1}{t_2} = (\frac{V_1}{V_2})^N exp[\frac{E_s}{k}(\frac{1}{T_1} - \frac{1}{T_2})] \quad \textbf{6-1}$$

where E_s is a pseudo-activation energy, N is the voltage acceleration factor, and k is the Boltzman constant [8]. 1 and 2 represents different test conditions.

10 μm OA-10G glass with sputtered Pt electrodes (diameter = 10 mm dots) has been tested for HALT studies (Error! Reference source not found.**a**). Five sample were put under the contact p robes in the furnace, and all other probes were insulated with alumina as shown in Error! Reference source not found.**b**. A schematic representation of the HALT test was shown in Error! Reference source not found., 1000 V was applied on the samples through a Trek amplifier (model number

2220) and the current from each sample position was recorded by an Agilent Pico-ammeter (HP 4140 pA meter). The furnace temperature was kept at 250 ^{o}C. All samples broke after about 24 hrs.

Based on this study, the breakdown of the low-alkali boroaluminosilicate glass is attributed to the movement of the sodium ions, thus an E_s of 0.93 eV is assumed based on the calculation result of Dash [9]. According to the desired DC bus capacitor specifications for inverters (Error! R eference source not found.), the MTTF for 140 ^{o}C and 600 V could be calculated based on **equation** 6-1 and the lifetime is predicted to be 2090 hrs.

(a)

(b)

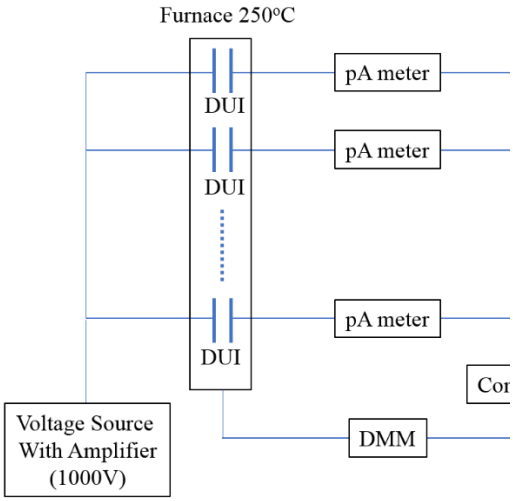

(c)

Figure 6-3: (a) HALT test instrument. (b) HALT furnace showing multiple sample stages and contact probes. (b) Schematic representation of the HALT set up. DMM= Digital Multimeter, DUT = Device Under Test.

In **Figure 4-4** we found out that the Weibull modulus β decreased at 200 ºC compared to room temperature. This is worth exploring with the HALT system to study the temperature effect on the stability of the glass and polymer-glass laminates. This could be done in correlate with the simulation of streamer model to further study the electric field / temperature effect as well.

6.4 References

1. Kendall, K., et al., Influence of toughness on Weibull modulus of ceramic bending strength. *Journal of Materials Research*, 1986. **1**(1): p. 120-123.

2. Roy, A., et al., Improvement in mechanical properties of jute fibres through mild alkali treatment as demonstrated by utilisation of the Weibull distribution model. *Bioresource technology*, 2012. **107**: p. 222-228.

3. Sarkarat, M., et al., Enhanced mechanical stability of high temperature ultra-thin glass/polymer composite dielectrics. *Materials Letters*, 2017. **208**: p. 10-13.

4. Wilcox, D.I., et al., 63.1: Biaxial Stress in Thin Glass during Ring-on-Ring Testing with Large Deflections. *SID Symposium Digest of Technical Papers*, 2013. **44**(1): p. 874-876.

5. Salem, J., et al., Standard Test Method for Monotonic Equibiaxial Flexural Strength Testing of Advanced Ceramic at Ambient Temperature. Draft Rev, 2000. **4**.

6. Cotterell, B., et al., The Strength of the Silicon Die in Flip-Chip Assemblies. *Journal of Electronic Packaging*, 2003. **125**(1): p. 114.

7. Prokopowicz, T. and A. Vaskas, Research and development intrinsic reliability subminiature ceramic capacitors. 1969, SPRAGUE ELECTRIC CO NORTH ADAMS MA.

8. Dash, P., Dynamics of Space Charge Polarization and Electrical Conduction in Low Alkali Boroaluminosilicate Glasses. 2013.

VITA

Mengxue Yuan

Mengxue Yuan was born of November 17th, 1989, in Leshan China, to Mrs. Ruijun Yuan and Mr. Bin Diao. Mengxue went to elementary school in Chengdu, China with her mother continuing her medical school education. After finishing her high school in 2009, she got admitted to the China University of Petroleum (East China) where she completed her bachelors with a major in chemical engineering and a minor in English. After graduating with her bachelor's degrees in 2013, she joined Penn State to pursue her Doctorate in the Materials Sciences and Engineering department.

SELECTED PUBLICATIONS (first and co-first author):

Yuan, M., Li, B., Zhang, S., Rajagopalan, R., & Lanagan, M. T. (2020). High-Field Dielectric Properties of Oriented Poly (vinylidene fluoride-co-hexafluoropropylene): Structure–Dielectric Property Relationship and Implications for Energy Storage Applications. *ACS Applied Polymer Materials*, *2*(3), 1356-1368.

Yuan, M., Zhang, G., Li, B., Chung, M., Rajagopalan, R., & Lanagan, M. T. (2020). Thermally-stable low-loss polymer dielectrics enabled by attaching crosslinkable antioxidant to polypropylene. *ACS Applied Materials & Interfaces*,*12* (12), 14154-14164.

Yuan, M., Rajagopalan, R., Lanagan, M., & Zhang, S. (2019). High electrical reliability glass-polymer laminates. *IEEE Transactions on Dielectrics and Electrical Insulation*, *26*(3), 885-889.

Mengxue Yuan, Maryam Sarkarat, Shihai Zhang, Ramakrishnan Rajagopalan, and Michael T. Lanagan. " Electrical Reliability of Polymer Enhanced Glass Dielectrics. "*US-Japan Conference Proceedings, 2017*

Yuan, M., Zhang, S., Rajagopalan, R., & Lanagan, M. (2016, October). High field dielectric properties of polymer-glass laminate. In *2016 IEEE Conference on Electrical Insulation and Dielectric Phenomena (CEIDP)* (pp. 474-477). IEEE.

Li, B., Yuan, M., Zhang, S., Rajagopalan, R., & Lanagan, M. T. (2018). Abnormal high voltage resistivity of polyvinylidene fluoride and implications for applications in high energy density film capacitors. *Applied Physics Letters*, *113*(19), 193903.